Geophysical Prospecting

Geophysical Prospecting

ORIGINAL ARTICLE OPEN ACCESS

Viscoacoustic Full Wavefield Migration With Tomographic Q Estimation

Mohammad Safari | Dirk Jacob Verschuur

Department of Geoscience & Engineering, TU Delft, Delft, The Netherlands

Correspondence: Mohammad Safari (M.safari@tudelft.nl)

Received: 20 August 2025 | **Revised:** 21 April 2026 | **Accepted:** 6 May 2026

Keywords: inversion | seismic imaging | tomography | *quality factor*

ABSTRACT

Seismic wave propagation in the Earth's subsurface is influenced by anelastic attenuation, which causes energy loss and waveform distortion, degrading image resolution. This effect, quantified by the quality factor (Q_f), is particularly pronounced in settings such as carbon capture and storage and near-surface studies, where fluids, gases or unconsolidated sediments are present. Conventional Q_f estimation methods – such as spectral ratio and centroid frequency shift – often rely on simplifying assumptions, have limitations in heterogeneous media and produce smeared Q_f results. We address these limitations by integrating attenuation compensation and Q_f estimation directly into the full wavefield migration framework. Our method embeds Q_f into a one-way forward modelling operator and applies full-waveform matching on residual data to estimate attenuation, compensating for it during migration. Implemented in the image domain within a wave-equation tomography framework, it links model and Q_f perturbations for robust, localized estimation. Tests on synthetic and field data confirm that the approach accurately recovers both reflectivity and attenuation models, improving resolution and producing more geologically consistent images. Compared with conventional spectral-based Q_f estimation methods, the proposed full-waveform matching framework jointly estimates reflectivity and attenuation during migration while maintaining control over internal multiples.

1 | Introduction

Seismic wavefields propagating through the subsurface are influenced by a range of attenuation phenomena, resulting in pronounced energy dissipation and waveform alteration. Accurate characterization and compensation of the attenuation within the overburden are critical for enhancing the resolution and reliability of seismic imaging and inversion methodologies. Geometric spreading represents one such effect and is typically addressed in most migration algorithms. In addition, reflection and transmission phenomena introduce amplitude variations in the wavefield as a result of impedance contrasts within the medium. Anelastic attenuation of P-waves, characterized by the quality factor (Q_f), leads to a gradual reduction of wave energy with increasing propagation distance or time. Lower values of Q_f correspond to greater energy loss per wave cycle, indicating stronger attenuation. It is important to note that such large-scale anelastic behaviour often originates from the cumulative action of small-scale elastic processes, such as grain boundary friction, fluid flow or microcracking. Moreover, attenuation is intrinsically associated with dispersion, wherein energy shifts towards lower frequencies, resulting in waveform broadening and distortion over time (Aki and Richards 2002).

Accurate estimation of Q_f provides key insights into subsurface properties such as lithology and the presence of fluids or gases – essential for exploration, monitoring and emerging applications like carbon capture and storage (CCS). Laboratory and rock physics studies on CO_2 monitoring have shown that seismic velocities and attenuation can vary significantly following CO_2

injection (Carcione et al. 2006; Huang et al. 2023; Dong et al. 2025). Therefore, developing reliable methods to account for attenuation effects in imaging is crucial for ensuring accuracy in these applications.

In the field of seismic attenuation estimation using seismic reflection data and sonic logs, several methods have been developed over the years. The classical spectral ratio method (White 1992) compares the spectral content of seismic signals at different depths to derive attenuation characteristics. Another approach is the centroid frequency shift (CFS) method (Quan and Harris 1997). This method involves correlating the quality factor, Q_f, with changes in the centroid frequency of the seismic wavelet. Then the complex spectral ratio (CSR) method (Cheng and Margrave 2008) was developed to address some of the limitations seen in earlier approaches. It combines elements of the spectral ratio and CFS methods. The CSR method estimates Q_f based on the constant-Q_f theory, relating to the spectral properties of the wavelet at two different depth levels. Another method is the Q_f-inversion method (Raji and Rietbrock 2013), which is particularly focused on estimating Q_f from real seismic data. This method starts with isolating two different reflectors using a Hanning window, and then computing the Fourier transform within this window to analyse the captured signal.

In reality, the quality factor Q_f varies across different spatial areas, much like how a velocity field is distributed. Traditional one-dimensional inverse Q_f filtering, which processes seismic data trace by trace, does not fully capture how seismic waves move through complex geological structures. Therefore, it is essential to correctly implement absorption compensation within the migration scheme, as this scheme is adept at precisely handling the complexities of wave paths. In the process of Q_f migration, and particularly when estimating propagation operators, the waveform is subject to attenuation as it propagates forward. This affects the wavelet's shape. Without adequate compensation for this attenuation, its effects will be transferred to the reflector, resulting in a dispersed pulse.

Several studies have examined Q_f-migration in prestack and poststack settings, addressing absorption and dispersion within their schemes, including those by Mittet et al. (1995), Yu et al. (2002), C. Zhang (2008) and Wang (2008). Also, a wide range of inversion-based Q_f tomography methods have been developed to account for attenuation effects, most of which perform attenuation measurements in the data domain and rely on spectral analysis techniques such as the spectral ratio or CFS methods. These include the works of Tonn (1991), Quan and Harris (1997), Dasgupta and Clark (1998), Mateeva (2003), Plessix (2006), Rickett (2007) and Reine et al. (2012), as well as more recent efforts using wave-equation tomography or full-waveform inversion (e.g., Kamei and Pratt 2008; Bai and Yingst 2013; Wang 2014; Dutta 2016; Dutta and Schuster 2016).

Despite their methodological differences, these approaches share a reliance on amplitude spectral characteristics to infer Q_f. Such spectral ratio and CFS methods are typically based on local, approximately one-dimensional assumptions and are sensitive to bandwidth selection, noise and frequency-dependent attenuation. Previous studies have shown that spectral ratio estimates can be significantly biased in the presence of frequency-dependent Q_f (Gurevich and Pevzner 2015; Y. Zhang et al. 2015), and that both spectral ratio and CFS methods may fail to detect localized attenuation anomalies in heterogeneous media (Carvalho Costa and Gomes 2011). As a result, spectral-ratio-based methods provide spatially averaged attenuation estimates, whereas full-waveform matching exploits the complete wavefield to map attenuation effects in a tomographic manner, leading to improved spatial localization of Q_f. They often simplify wave propagation by neglecting the complexities of full-waveform modelling and by relying on synthetic or reference models, which limits their effectiveness in heterogeneous media. Additionally, they tend to produce smeared Q_f results, leading to Q_f estimates that are generally not well-localized.

In a more recent work, Shen et al. (2018) developed a spatially varying quality factor Q_f model for gas clouds/pockets and introduced the wave-equation migration Q_f analysis. This inversion-based method operates in the image space, directly correlating changes in the Q_f model with image alterations. However, the reflectivity image itself is not updated during the inversion; instead, Q_f is inferred from spectral attributes extracted from migrated images. It also utilizes wave-equation-based Q_f tomography to manage complex wave propagation. However, their method still relies on spectral ratio measurements from migrated images rather than using full-waveform matching. Wave-equation Q_f tomography methods, such as Dutta (2016) and Dutta and Schuster (2016), operate in the data domain and update Q_f through adjoint-state waveform gradients governed by two-way wavepath sensitivities; the proposed approach performs Q_f estimation in the image domain through migration-driven full-waveform matching.

In parallel with efforts focused on estimating the quality factor, significant progress has been made in Q_f-compensated imaging and inversion frameworks, where attenuation effects are incorporated into wave-equation modelling and migration operators to improve image fidelity. Examples include Q_f-compensated full-waveform inversion approaches for multiparameter estimation, such as velocity and density (Wang and Qu 2022), as well as least-squares reverse time migration methods that integrate Q_f compensation within migration imaging, including elastic and ocean-bottom seismic implementations (Y. Zhang et al. 2024; Qu et al. 2021, 2022). These approaches demonstrate the growing maturity of Q_f-aware imaging, but they typically rely on a prescribed Q_f model rather than performing direct or tomographic Q_f estimation.

While conventional Q_f-estimation methods often rely on frequency-domain spectral analysis, this paper presents a tomographic approach that utilizes full-waveform matching for more accurate Q_f-estimation. Our method operates on the residuals between observed and modelled data and incorporates attenuation compensation within a least-squares migration framework. We used the full wavefield migration (FWM) method (Berkhout 2014b; Davydenko and Verschuur 2017) as the imaging engine and enhanced its ability to deliver higher seismic resolution in geologically complex areas. The FWM uses the full wavefield modelling (FWMod) (Berkhout 2014a) scheme, which includes geometric spreading, reflectivity and transmission effects and all multiple scattering by recursively and iteratively propagating wavefields up/down in the subsurface.

This modelling engine is optimized for an inversion algorithm that uses the subsurface's propagation velocity and reflectivity models based on measured seismic data. The inversion algorithm uses a gradient descent scheme, where the difference between measured and modelled data is projected onto updates for the reflectivity model. Because of the modular set-up of the FWMod process, where propagation and reflection/transmission are described by wavefield operators, bringing in the Q_f-effect is relatively simple, by redefining the propagator (Safari and Verschuur 2023, 2024, 2025).

We used FWM in this study not only for its ability to incorporate attenuation effects but also for its full control over internal multiples. Internal multiples occurring within subsurface layers are often considered as noise in seismic processing. Using FWM, which inherently models and manages internal multiples, we ensure that the inversion process remains robust without requiring explicit suppression or removal of these events. This highlights the flexibility and strength of the proposed approach in handling complex wave phenomena within the subsurface.

In this method, we adopt an approach for updating Q_f that is inspired by the velocity update process in the joint migration inversion (JMI) (Staal and Verschuur 2013; Berkhout 2014c; Verschuur et al. 2016). Within this framework, perturbation theory is employed to relate image perturbations to perturbations in Q_f. Accordingly, Q_f updates are localized in the image domain rather than being distributed along wavepaths or inferred from spectral attributes. Our method achieves robust and localized Q_f estimation by integrating Q_f in a one-way modelling operator, using full waveform matching. It is fully tomographic, overcoming the limitations of conventional techniques.

The structure of this paper is as follows. We begin in Section 2 with a review of the notation and fundamentals of FWM and also introduce our desired quality factor (Q_f) model. Section 3 then describes how Q_f is incorporated into full waveform modelling, followed in Section 4 by the approach for estimating Q_f values. Section 5 outlines the inversion framework, while Section 6 demonstrates the approach using synthetic and field data examples. Finally, Section 7 summarizes the main conclusions of the study.

2 | Notations and Review

The aim of FWM is to fit observed seismic data with a model by minimizing the difference between them, referred to as the residual energy, which serves as the objective function in the data-fitting process. The key parameters in the inversion process are the propagation velocity model and the seismic reflectivity model. Using these parameters, the FWMod scheme can regenerate seismic data, including primary reflections and internal multiples. Within this framework, phase changes are accounted for by a smooth velocity model, while amplitude changes are captured through reflectivities. This approach aligns with standard practices in migration algorithms. However, FWM extends beyond the norm by incorporating a two-way scattering component, which additionally accounts for transmission effects and multiple scatterings. This inclusion renders FWM as more comprehensive and accurate representation of wave propagation compared to conventional wave-equation migration methods (Claerbout 1971; Gazdag 1978). In this paper, we use specific notation for key concepts to ensure clarity. The notation Q_f refers to the quality factor, a significant parameter in our study. Additionally, we use Q_w to denote the total upgoing or downgoing wavefield. These notations are used throughout the article for consistency and to avoid any potential confusion between these two distinct concepts.

2.1 | Full Wavefield Modelling

The FWMod is the forward modelling engine in the FWM process. This engine effectively decouples velocity and reflectivity (Berkhout 2014a). On the one hand, scattering is generated by the reflectivity model, which is the parameter that the scheme attempts to estimate for explaining the observed data. On the other hand, the velocity profile affects only the kinematics. We describe and demonstrate the FWMod process for the two-dimensional (2D) case; however, the method can easily be extended to the full three-dimensional situation, as described in Davydenko and Verschuur (2017). We also limit to the case without wave conversions, although FWMod allows such an extension (Berkhout 2014a; Hoogerbrugge and Verschuur 2021). When a monochromatic wavefield $\vec{P}^{+}(z_n)$ going downwards reaches a sharp boundary at depth z_n and gets reflected, we can describe the reflected wavefield in the frequency domain using the reflection operator $\mathbf{R}^{\cup}(z_n)$:

$$\vec{Q}_w^{-}(z_n) = \mathbf{R}^{\cup}(z_n)\vec{P}^{+}(z_n), \tag{1}$$

where the reflection operator contains spatial convolution operators that describe the local reflection properties (Davydenko and Verschuur 2017). For angle-independent reflection, this operator has a diagonal structure. The upgoing wavefield at depth level z_n comprises not only energy from the reflected wavefield but also from the transmitted wavefield at the discontinuity. Therefore, we can express

$$\vec{Q}_w^{-}(z_n) = \mathbf{T}^{-}(z_n)\vec{P}^{-}(z_n) + \mathbf{R}^{\cup}(z_n)\vec{P}^{+}(z_n), \tag{2}$$

in which $\vec{Q}_w^{-}(z_n)$ represents the total upgoing wavefield, which is moving away from the discontinuity. The term $\vec{P}^{-}(z_n)$ describes the incoming upgoing wavefield at depth level z_n from below, as illustrated in Figure 1. Additionally, $\mathbf{T}^{-}(z_n)$ denotes the transmission operator at the discontinuity. The transmission operators are defined by the equation $\mathbf{T}^{\pm}(z_n) \equiv \mathbf{I} + \boldsymbol{\delta}\mathbf{T}^{\pm}(z_n)$. Here, $\boldsymbol{\delta}\mathbf{T}^{\pm}(z_n) = 0$ implies that there is no contrast at depth z_n. Following this definition, Equation (2) is expressed as

$$\vec{Q}_w^{-}(z_n) = \vec{P}^{-}(z_n) + \boldsymbol{\delta}\mathbf{T}^{-}(z_n)\vec{P}^{-}(z_n) + \mathbf{R}^{\cup}(z_n)\vec{P}^{+}(z_n), \tag{3}$$

where the last two terms represent the scattered wavefields at depth level z_n, accounting for the wavefields arriving from both sides. Similarly, the total downgoing wavefield $\vec{Q}_w^{+}(z_n)$, which departs from depth level z_n, can be formulated as the summation of transmission and reflection components

$$\begin{aligned}\vec{Q}_w^{+}(z_n) &= T^{+}(z_n)\vec{P}^{+}(z_n) + R^{\cap}(z_n)\vec{P}^{-}(z_n)\\ &= \vec{P}^{+}(z_n) + \delta T^{+}(z_n)\vec{P}^{+}(z_n) + R^{\cap}(z_n)\vec{P}^{-}(z_n).\end{aligned} \tag{4}$$

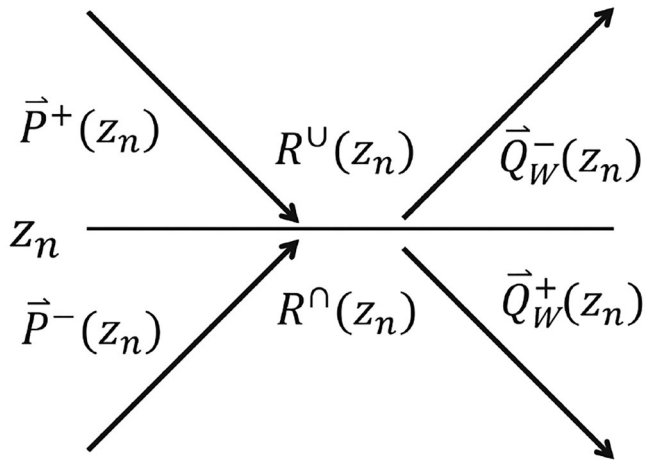

Figure 1 | Schematic representation of reflection at both sides of a depth level.

The wavefields $\vec{Q}_w^{\pm}(z_n)$ undergo transmission and reflection processes at depth z_n and subsequently propagate to the neighbouring depth levels $z_{n\pm1}$. This propagation is facilitated by wavefield extrapolation, which is based on the principles of the Rayleigh II integral:

$$\vec{P}^{\pm}(z_{n\pm1}) = \mathbf{W}^{\pm}(z_{n\pm1}; z_n)\vec{Q}_w^{\pm}(z_n). \tag{5}$$

In this formulation, $\mathbf{W}^+(z_{n+1}; z_n)$ and $\mathbf{W}^-(z_{n-1}; z_n)$ denote the downgoing and upgoing propagation operators, respectively, which are used to propagate the wavefields to the subsequent depth level, $z_{n\pm1}$. The components of $\mathbf{W}$ can be related to the dipole Green's function as follows (see also Berkhout 1982):

$$W_{i,j}(z_m; z_n) = 2\,\mathrm{sign}(z_n - z_m)\frac{\partial G}{\partial z}(x_j, z_m; x_i, z_n), \tag{6}$$

where $G(x_j, z_m; x_i, z_n)$ represents a Green's function that connects the wavefield's original position at (x_j, z_m) to its new location after propagation at (x_i, z_n). In a homogeneous layer, the matrix $\mathbf{W}$ exhibits a Toeplitz structure. This implies that we can directly relate a column of the propagation operator $\mathbf{W}$ to the phase-shift operator:

$$\vec{W}_j(z_m; z_n) = \mathcal{F}_x^{-1}\left[\mathrm{e}^{-jk_z\Delta z}\mathrm{e}^{-jk_x x_j}\right], \tag{7}$$

with, for the 2D case,

$$k_z = \sqrt{k^2 - k_x^2}, \tag{8}$$

where $\mathcal{F}_x$ represents a spatial Fourier transform, x_j is the source position of the Green's function, k is the wavenumber and $\Delta z = |z_n - z_m|$. The wavenumber k can be expressed as the ratio of angular frequency (ω) to the velocity (c), given by the equation $k = \frac{\omega}{c}$. For laterally inhomogeneous media, each row of $\mathbf{W}$ represents a propagation operator that can still be obtained via 7 if we use the local propagation velocity, assuming smooth lateral variations. In the FWMod procedure, the scattering process, as outlined in Equations (3) and (4), and the propagation process, detailed in Equation (5), are iteratively executed at each depth level. The procedure can be summarized in the following equations (Berkhout 2014a):

- for the downgoing wavefields ($m = 1,2,\ldots,M$):

$$\vec{P}^+(z_m) = \underline{\mathbf{W}}^+(z_m; z_0)\vec{S}^+(z_0) + \sum_{n=0}^{m-1}\underline{\mathbf{W}}^+(z_m; z_n)\mathbf{R}^\cap(z_n)\vec{P}^-(z_n), \tag{9}$$

with

$$\underline{\mathbf{W}}^+(z_m; z_0) = \mathbf{W}^+(z_m; z_{m-1})\prod_{l=m-1}^{n+1}\mathbf{T}^+(z_l)\mathbf{W}^+(z_l; z_{l-1}), \tag{10}$$

- for the upgoing wavefields ($m = 0,1,\ldots,M-1$):

$$\vec{P}^-(z_m) = \underline{\mathbf{W}}^-(z_m; z_0)\vec{P}^-(z_M) + \sum_{n=m+1}^{M}\underline{\mathbf{W}}^-(z_m; z_n)\mathbf{R}^\cup(z_n)\vec{P}^+(z_n), \tag{11}$$

with

$$\underline{\mathbf{W}}^-(z_m; z_0) = \mathbf{W}^-(z_m; z_{m+1})\prod_{l=m+1}^{n-1}\mathbf{T}^-(z_l)\mathbf{W}^-(z_l; z_{l+1}), \tag{12}$$

where $\vec{S}^+(z_0)$ is the downgoing source wavefield at the surface.

When we start the modelling procedure with the assumption that $\vec{S}^+(z_0)$ and $\mathbf{R}$ are known at all depth levels, we set $\vec{P}^+(z_m) = 0$ and $\vec{P}^-(z_m) = 0$ at each depth level z_m. Utilizing Equation (9), we can subsequently compute the value of $\vec{P}^+(z_m)$ for each depth level, followed by the update of $\vec{P}^-(z_m)$ using Equation (11). After a single evaluation of Equations (9) and (11), we complete one 'roundtrip' and obtain all primary reflection responses. Subsequent roundtrips introduce higher order scattering effects (multiples) into the results.

2.2 | Quality Factor Model

Anelastic attenuation, which is quantified by the quality factor (Q_f), reflects the energy loss of seismic waves as they travel over distance or time. The Q factor is a dimensionless measure of this anelasticity. It is defined as

$$Q_f = \frac{-2\pi E}{\Delta E}, \tag{13}$$

where E represents the energy stored in the system at the maximum strain and ΔE is the energy lost in each cycle due to anelastic attenuation. Because ΔE is negative, as it represents a loss of energy, a minus sign is required to map it to a positive Q_f value. The inverse of the quality factor, denoted as Q_f^{-1}, is a measure of the portion of energy lost during each cycle or wavelength. This can be expressed as

$$Q_f^{-1} = \frac{-\Delta E}{2\pi E}, \tag{14}$$

which implies that a higher Q_f indicates lower energy loss (or higher energy conservation) and vice versa. In seismic analysis, it

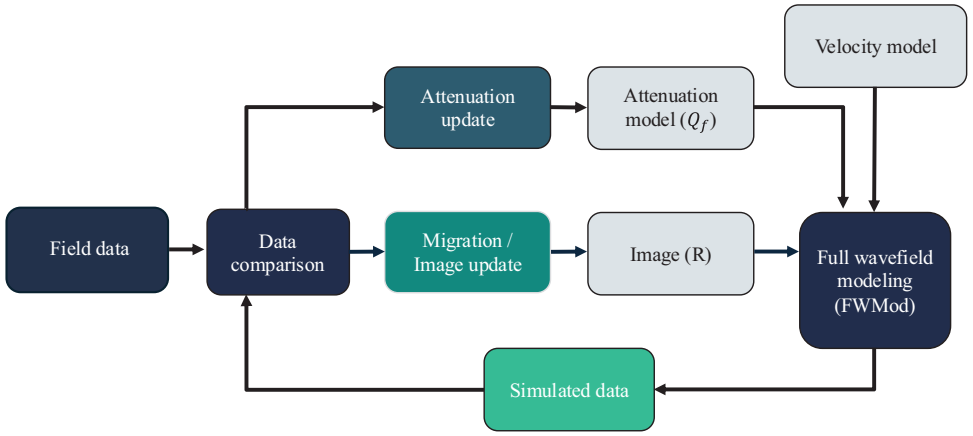

Figure 2 | Flow diagram related to the closed-loop Q-FWM process, where we alternate between Q_f updates and image updates.

is commonly accepted that the quality factor Q_f does not change much within the range of seismic frequencies (Aki and Richards 2002). Therefore, in our work, we use a nearly constant Q_f model (Futterman 1962) to estimate seismic wave attenuation during migration, which operates under the consideration that Q_f is almost frequency-independent. The one-way wave equation for viscoacoustic modelling, introduced by Futterman (1962), looks similar to the acoustic wave equation, but it uses a complex number to represent slowness, as follows:

$$s_c = s\left(1 - \frac{1}{\pi Q_f}\ln\left(\frac{\omega}{\omega_0}\right)\right)\left(1 + \frac{i}{2Q_f}\right). \tag{15}$$

Equation (15) introduces the variables s_c, s, ω_0, which are the complex slowness, the slowness without attenuation effect and the central angular frequency, respectively. We can take the attenuation factor (A) as the inverse of the Q_f value, where A is defined as $1/Q_f$. This simplification facilitates the derivation process and changes Equation (15) as follows:

$$s_c = s\left(1 - \frac{A}{\pi}\ln\left(\frac{\omega}{\omega_0}\right)\right)\left(1 + \frac{iA}{2}\right). \tag{16}$$

Equation (16) combines the slowness and the attenuation parameter to model wave propagation that accounts for anelastic attenuation effects (Toksöz et al. 1981; Sheriff and Geldart 1995; Aki and Richards 2002). Note that even if Q_f or A is taken frequency independent, its effect on wave propagation is still frequency dependent.

3 | Incorporating Q_f in Full Waveform Modelling

Including the anelastic attenuation effect in one-way propagators within the full wavefield modelling engine is straightforward. The FWMod employs one-way propagators, usually based on the phase-shift operators, for example, via the phase-shift plus interpolation methodology (Gazdag and Sguazzero 1984b). As was shown in Equations (7) and (8), and, taking $x_j = 0$, the involved phase shift operators in the wavenumber domain for 2D can be written as

$$W(k_x, \omega) = \mathrm{e}^{-jk_z\Delta z}, k_z = \sqrt{\omega^2 s^2 - k_x^2}, \tag{17}$$

with Δz the extrapolation distance, this equation can be easily extended to include the complex slowness as given by

$$W(k_x, \omega) = \mathrm{e}^{-j\sqrt{\omega^2\left(s\left(1-\frac{A}{\pi}\ln\left(\frac{\omega}{\omega_0}\right)\right)\left(1+\frac{iA}{2}\right)\right)^2 - k_x^2}\Delta z}, \tag{18}$$

which provides the expected frequency-dependent amplitude and phase effects. By using the new propagation operator, as shown in Equation (18), we enhanced the effectiveness of FWM by incorporating the Q_f into its forward modelling engine, FWMod. At this point in the study, if the Q_f model is available, it can be utilized during the migration process to compensate for Q_f.

4 | Estimation of Q_f Values in FWM

Although having an accurate Q_f model can improve inversion outcomes, it is often impractical to obtain one. Measuring the Q_f precisely in seismic data analysis remains a challenging task, yet it is crucial for interpreting subsurface features. By integrating Q_f estimation as a core component of the FWM process, our approach eliminates the need for pre-existing Q_f models and enhances the accuracy and reliability of inversion results. The method for estimating and updating the Q_f shares many similarities with the velocity update process in JMI (Staal and Verschuur 2013; Berkhout 2014c; Verschuur et al. 2016). The JMI constitutes a tomographic problem, where we combine wavefields travelling in the same direction and aim to simultaneously determine the reflectivity and velocity of the subsurface from seismic recordings. This is achieved through a gradient descent scheme that minimizes the difference between modelled data and the seismic recordings in a least-squares sense. To convert data mismatches into updates for reflectivity or velocity, their relationship has been linearized, known as perturbation theory. Similarly to JMI, initially, a linear relationship must be established between the propagation operators and the attenuation model by considering their respective perturbations. Unlike in the case of velocity, where derivatives are taken with respect to velocity or slowness, here we take the derivative with respect to the attenuation (A) value, which is more practical than using Q_f.

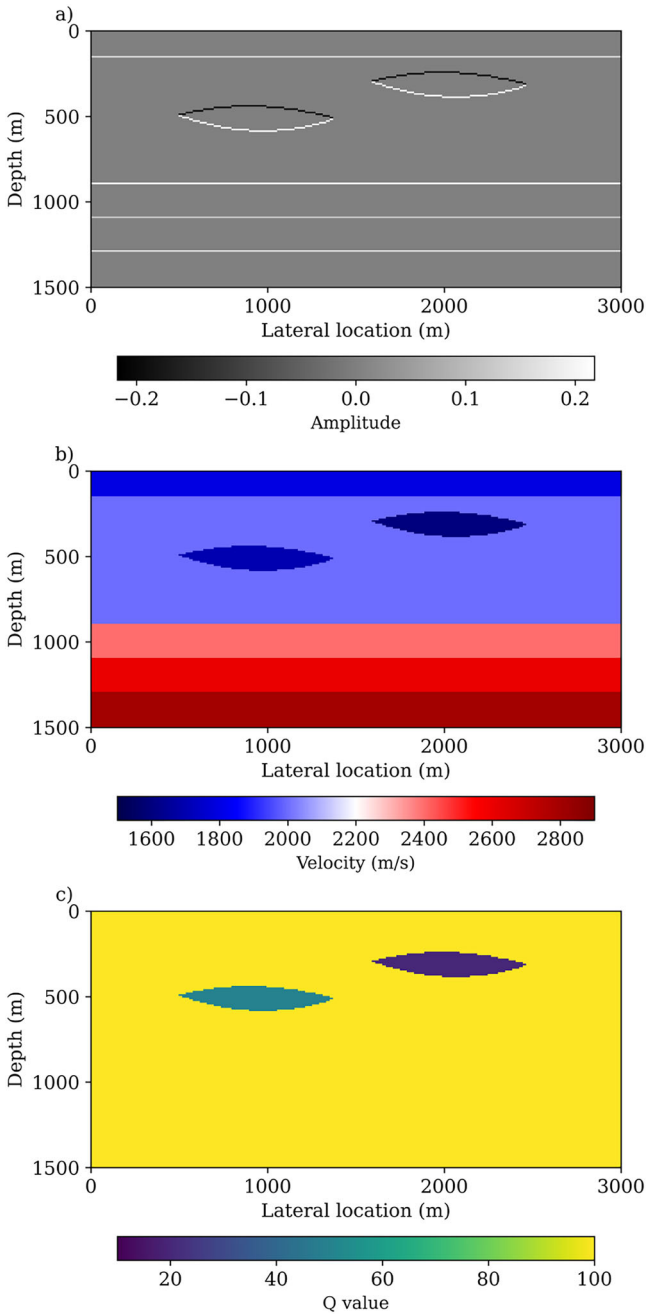

Figure 3 | Models used for generating synthetic seismic data: (a) true reflectivity model, (b) true velocity model and (c) true Q_f model.

4.1 | Propagation Perturbations

As shown before, to incorporate the attenuation effect in FWMod, we replaced the normal slowness with complex slowness, as shown in Equation (18). Given that in the FWMod formulation, the attenuation model only affects phase changes during wave extrapolation, which is governed by the extrapolation operator $\mathbf{W}$, an attenuation perturbation then affects the extrapolation operators $\mathbf{W}^-$ such that

$$\mathbf{W}^-(z_m, z_n) = \mathbf{W}_0^-(z_m, z_n) + \Delta\mathbf{W}^-(z_m, z_n), \tag{19}$$

where $\mathbf{W}_0^-$ represents the extrapolation operator as defined within the background medium and $\mathbf{W}^-$ denotes the operator defined in the true medium. Previously, it was established that a single column of the operator $\mathbf{W}^-$ can be calculated within the (k_x, ω) domain as follows:

$$\vec{W}_j^-(z_m; z_n) = \mathcal{F}_x^{-1}\left[\mathrm{e}^{-jk_z\Delta z}\mathrm{e}^{-jk_x x_j}\right], \tag{20}$$

where the vertical wavenumber k_z is defined through the complex slowness (Equation 16). Linearization of Equation (20) with respect to the attenuation parameter A leads to a linearized perturbation operator that relates attenuation perturbations to wavefield perturbations (Safari and Verschuur 2024). The detailed linearization procedure is provided in Appendix A. Following the linearization and stabilization procedures described in the Appendix, the resulting perturbation operator is given by

$$\vec{L}_{0j}^-(z_m, z_n) \approx \mathcal{F}_x^{-1}\left\{-j\Delta z\, k_0^2 \frac{k_z^*}{k_z^* k_z + \epsilon}\left[\left(1 - \frac{A}{\pi}\ln\frac{\omega}{\omega_0}\right)\left(1 + \frac{iA}{2}\right)^2\left(\frac{\ln(\omega/\omega_0)}{\pi}\right)^2 + \frac{i}{2}\left(1 + \frac{iA}{2}\right)\left(1 - \frac{A}{\pi}\ln\frac{\omega}{\omega_0}\right)^2\right]\mathrm{e}^{-jk_z\Delta z}\mathrm{e}^{-jk_x x_j}\right\}, \tag{21}$$

where the asterisk $*$ indicates complex conjugation and ϵ is a small positive stabilization parameter, the choice of which is described in Appendix A.3. Therefore, the (linearized) difference extrapolation operator can be expressed as follows:

$$\Delta\mathbf{W}^-(z_m, z_n) = \mathbf{L}_0^-(z_m, z_n)\Delta\mathbf{A}(z_n), \tag{22}$$

where $\Delta\mathbf{A}(z_n)$ is a diagonal matrix with the attenuation updates $\Delta\vec{A}(z_n)$ along its diagonal. The effect of attenuation perturbations at any point in the subsurface on the measured upgoing wavefield at the surface can be described as

$$\Delta\vec{P}_{\Delta A}^-(z_0) = \sum_{n=1}^{N}\underline{\mathbf{L}}_0^-(z_0, z_n)\Delta\mathbf{A}(z_n)\vec{Q}_w^-(z_n), \tag{23}$$

where

$$\vec{Q}_w^-(z_n) = \delta\vec{P}(z_n) + \sum_{m=n+1}^{N}\underline{\mathbf{W}}_0^-(z_m, z_m)\delta\vec{P}(z_m), \tag{24}$$

and

$$\underline{\mathbf{L}}_0^-(z_0, z_n) = \underline{\mathbf{W}}_0^-(z_0, z_{n-1})\mathbf{L}_0^-(z_{n-1}, z_n), \tag{25}$$

with $\mathbf{W}^-(z_0, z_0) = \mathbf{I}$.

4.2 | Reflectivity Perturbations

The reflectivity perturbation is kept unchanged, following the FWM approach of Davydenko and Verschuur (2017). In this approach, it is most effective to solve only for $\mathbf{R}^{\cup}$, which affects the amplitude of the reflected wave through Equation (3).

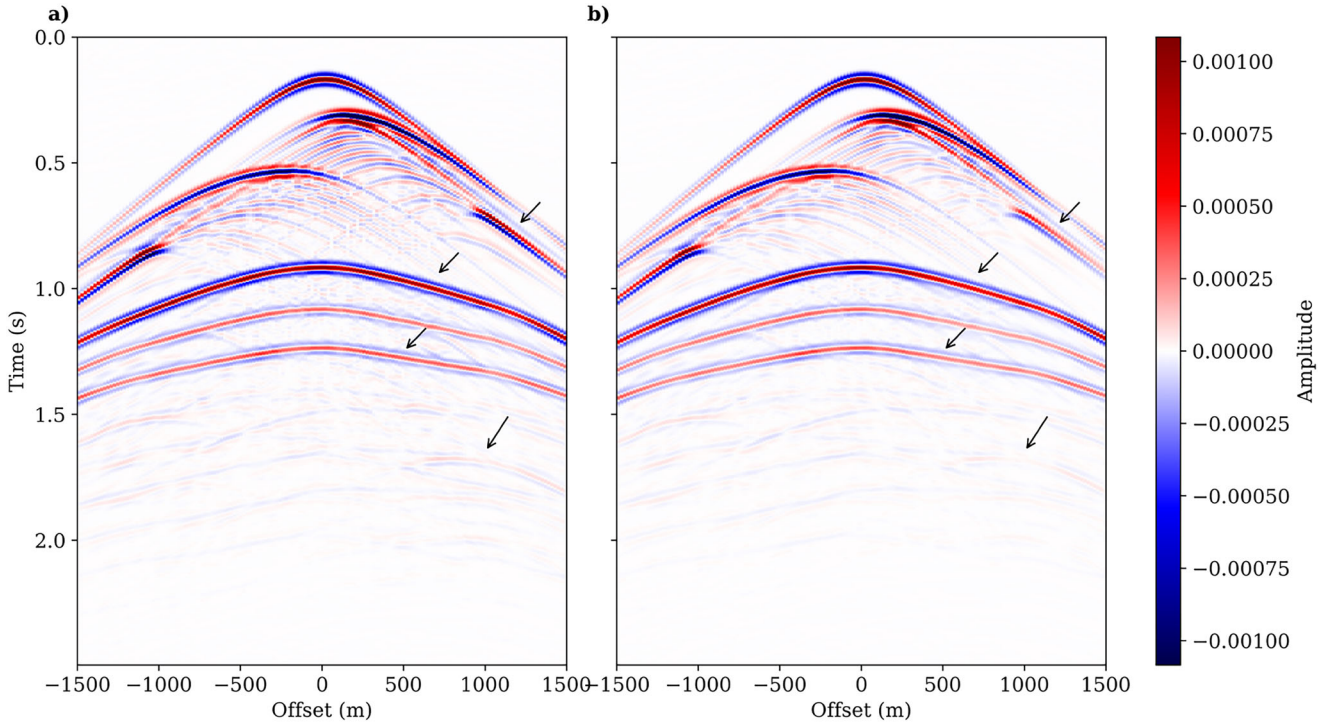

Figure 4 | Comparison of synthetic waveforms generated using (a) FWMod and (b) QFWMod. The inclusion of attenuation in QFWMod leads to reduced waveform amplitudes in deeper regions affected by high attenuation. The arrows indicate regions impacted by Q in panel (b).

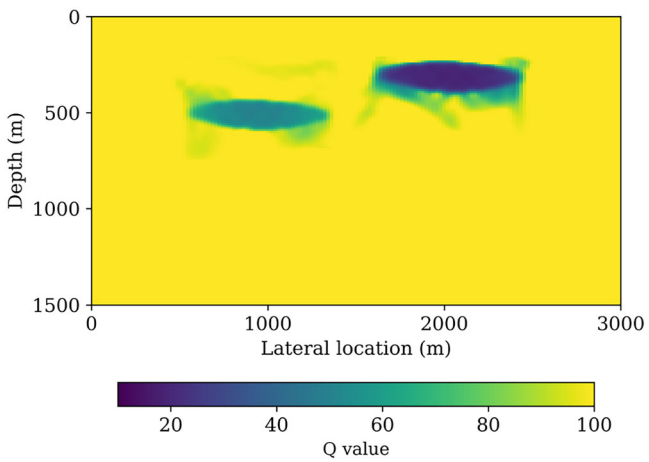

Figure 5 | Gradient test result; estimated Q_f model after 100 iterations of gradient-based inversion.

In this study, we do not consider the angle-dependency of reflectivities. This implies that all reflectivity operators $\mathbf{R}^{\cup}$ are diagonal matrices, where $\mathrm{diag}(\mathbf{R}^{\cup}(z_n, z_n)) = \vec{r}(z_n)$ represents the reflectivity values at depth level z_n along the spatial axis. A perturbed reflectivity operator can then be written as

$$\mathbf{R}^{\cup}(z_n) = \mathbf{R}_0^{\cup}(z_n) + \Delta\mathbf{R}(z_n), \tag{26}$$

in which $\mathbf{R}_0^{\cup}(z_n)$ represents the background reflectivity operator (i.e., the current estimate), $\mathbf{R}^{\cup}(z_n)$ represents the true reflectivity operator and $\mathrm{diag}(\Delta\mathbf{R}(z_n)) = \Delta\vec{r}(z_n)$ describes the difference. The influence of reflectivity perturbations at any subsurface point on the detected upgoing wavefield at the surface can then be described as follows:

$$\Delta\vec{P}^{-}_{\Delta r}(z_0) = \sum_{n=1}^{N} \underline{\mathbf{W}}^{-}(z_0, z_n)\Delta\mathbf{R}(z_n)\vec{P}^{+}(z_n). \tag{27}$$

5 | Inversion

Our proposed method aims to iteratively minimize the difference between the observed and simulated data through the implementation of a gradient descent strategy. The objective of this optimization process is to enhance the accuracy of the estimates of subsurface reflectivity and attenuation parameters. The target of this approach is summarized in the following objective function:

$$J = \sum_{\omega} \|\mathbf{P}^{-}_{\mathrm{obs}}(z_0) - \mathbf{P}^{-}_{\mathrm{mod}}(z_0)\|^2 = \sum_{\omega} \|\Delta\mathbf{P}^{-}(z_0)\|^2, \tag{28}$$

where each matrix $\mathbf{P}(z_0)$ represents the collection of all shot measurements $\vec{P}(z_0)$. Drawing from Equations (23) and (27), we are now equipped to derive the necessary gradients for implementing a gradient descent method:

$$\nabla\vec{r}(z_n) = \mathrm{diag}\left(\sum_{\omega}[\underline{\mathbf{W}}^{-}(z_n, z_0)]^{\mathrm{H}}\Delta\mathbf{P}(z_0)[\mathbf{P}^{+}(z_n)]^{\mathrm{H}}\right), \tag{29}$$

$$\nabla\vec{A}(z_n) = \mathrm{diag}\left(\sum_{\omega}[\underline{\mathbf{L}}^{-}(z_n, z_0)]^{\mathrm{H}}\Delta\mathbf{P}(z_0)[Q_w^{-}(z_n)]^{\mathrm{H}}\right), \tag{30}$$

where each gradient calculates a parameter update along depth level z_n and the operators $\underline{\mathbf{W}}$ and $\underline{\mathbf{L}}$ are based on the current attenuation and reflectivity estimates. We can now evaluate the

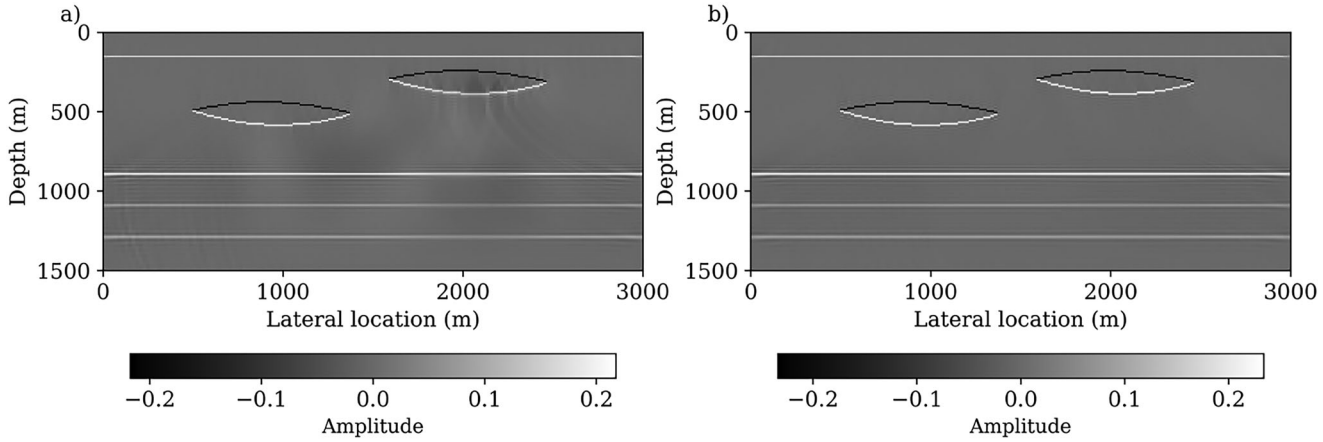

Figure 6 | Comparative analysis of reflectivity estimations across FWM and Q-FWM. (a) Estimated reflectivity by FWM. (b) Estimated reflectivity by Q-FWM.

wavefield perturbations predicted by these gradients:

$$\Delta\vec{P}^{-}_{\nabla r}(z_0) = \sum_{n=1}^{N} \underline{\mathbf{W}}^{-}(z_0, z_n)\nabla\mathbf{R}(z_n)\vec{P}^{+}(z_n), \tag{31}$$

$$\Delta\vec{P}_{\nabla A}(z_0) = \sum_{n=1}^{N} \underline{\mathbf{L}}^{-}_{0}(z_0, z_n)\nabla\mathbf{A}(z_n)\vec{Q}^{-}_{w}(z_n), \tag{32}$$

where $\nabla\mathbf{R}(z_n)$ and $\nabla\mathbf{A}(z_n)$ are square matrices, where the gradients $\nabla\vec{r}(z_n)$ and $\nabla\vec{A}(z_n)$ are positioned along their diagonals. After the gradients are calculated, the parameters are updated and the residual wavefields are slowly driven to a minimum level. When we are updating reflectivities, this means

$$r_{\text{new}}(x, z) = r_{\text{old}}(x, z) + \alpha\nabla r(x, z), \tag{33}$$

where

$$\alpha = \arg\min_{\alpha}\left(\sum_{\omega}\|\Delta\mathbf{P}^{-}(z_0) - \alpha\Delta\mathbf{P}^{-}_{\nabla r}(z_0)\|^2\right). \tag{34}$$

When we are updating the attenuations, we get

$$A_{\text{new}}(x, z) = A_{\text{old}}(x, z) + \beta\nabla A(x, z), \tag{35}$$

where

$$\beta = \arg\min_{\alpha}\left(\sum_{\omega}\|\Delta\mathbf{P}^{-}(z_0) - \beta\Delta\mathbf{P}^{-}_{\nabla A}(z_0)\|^2\right). \tag{36}$$

Notice that Equations (29)/(30) and (31)/(32) can be evaluated in a single depth recursion, using a scheme similar to the one described in Section 2.1. The flow diagram of the inversion process is shown in Figure 2.

6 | Examples

6.1 | Synthetic Data Example

To demonstrate the effectiveness of the proposed method, we first present a synthetic example. The test model consists of two lens-shaped anomalies with distinct attenuation characteristics, embedded within a weakly attenuating background. In seismic imaging, a quality factor Q_f greater than 100 generally corresponds to weak attenuation and several studies have shown that wavefield differences for $Q_f > 100$ are often negligible in typical exploration scenarios involving moderate frequencies and limited offsets (Hedlin 2006; Hauksson et al. 2006; Xing et al. 2019; Malinowski 2012). Based on this understanding, and to simplify the modelling while preserving physical realism, all $Q_f > 100$ are treated as equivalent to $Q_f = 100$ in our set-up. Accordingly, the background model is assigned a default $Q_f = 100$, while two lens-shaped anomalies are introduced to simulate attenuating bodies: the top-right anomaly is strongly attenuating, with $Q_f = 20$, and the second anomaly has a moderate attenuation value of $Q_f = 50$. Additionally, three reflectors are placed beneath the anomalies to enhance structural complexity, and one shallow reflector is included above them to simulate layered subsurface conditions.

Synthetic seismic data were generated using the Q_f model, the velocity model and the reflectivity structure shown in Figure 3a, 3b and 3c, respectively. The simulated frequency band spans 5–40 Hz, with a temporal sampling interval of 0.004 s and 512 time samples, and a Ricker wavelet with a 20 Hz peak frequency was employed. A common practice in selecting the reference frequency for the Futterman Q_f model is to use the central frequency or the highest frequency within the frequency band of the recorded data. For our numerical tests, we selected the central frequency, as it more accurately represents the dominant portion of our frequency band. As a demonstration of Q_f-based waveform modelling, the middle modelled shot record generated by FWMod is presented in Figure 4a, while the middle shot record generated using FWMod with attenuation (QFWMod) is shown in Figure 4b. Both simulations are performed using the same velocity and reflectivity models shown in Figure 3. In the presence of the high-attenuation zone on the right-hand side of the model, the waveforms generated by QFWMod exhibit a decay in amplitude with depth compared to the conventional FWMod results, as indicated by the arrows in Figure 4. This difference highlights the impact of attenuation on wavefield propagation and demonstrates the necessity of incorporating attenuation effects in waveform modelling. The acquisition geometry includes evenly spaced sources and receivers along the surface, with a maximum offset of 3000 m and a target depth of 1500 m. The spatial sampling

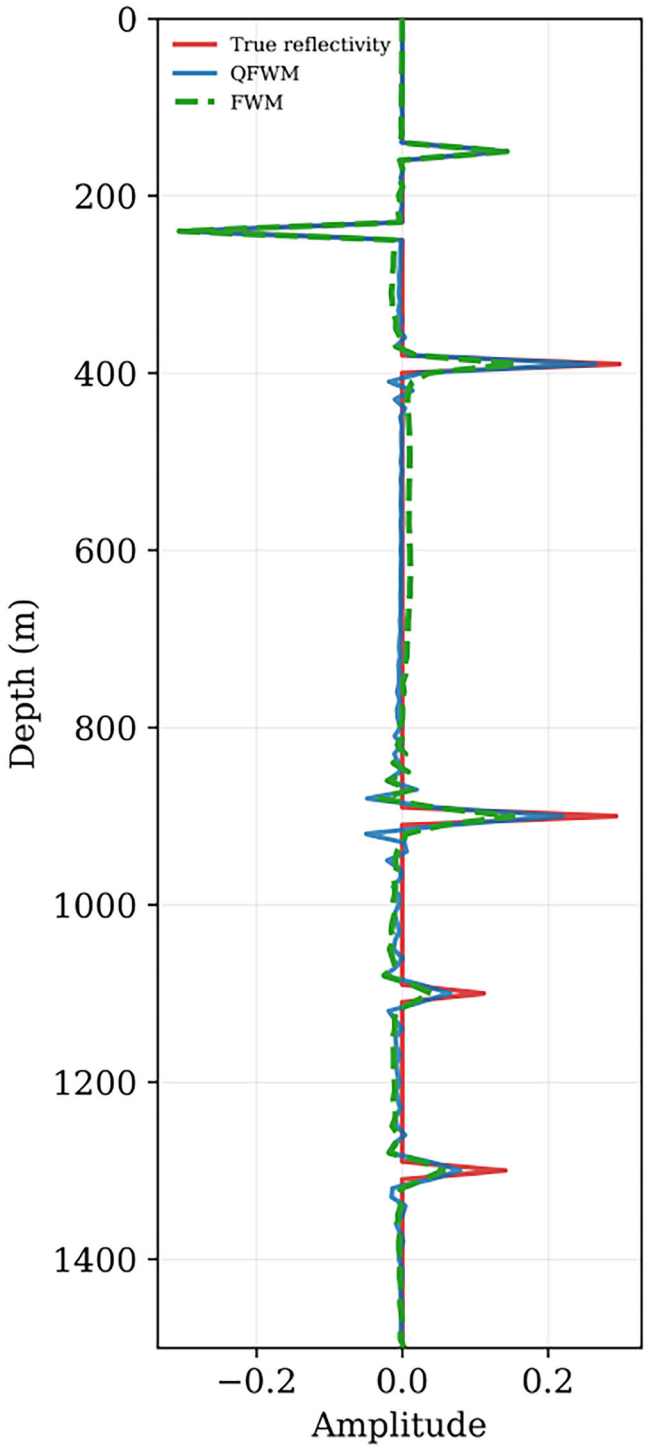

Figure 7 | Single-trace comparison among FWM, Q-FWM and the true reflectivity extracted at the same lateral position ($x = 2000$) along the vertical section.

intervals are 20 m horizontally and 10 m vertically. Internal multiples up to the third order are included, and all parameters are identical for FWMod and QFWMod. Note that Figure 4a is shown only for comparison, whereas shot records such as Figure 4b are used as input for viscoacoustic full wavefield migration with tomographic Q_f estimation (Q-FWM).

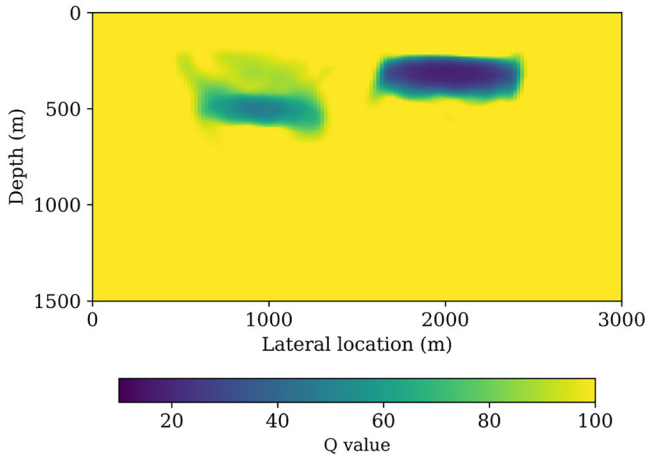

Figure 8 | The estimated Q_f model by Q-FWM.

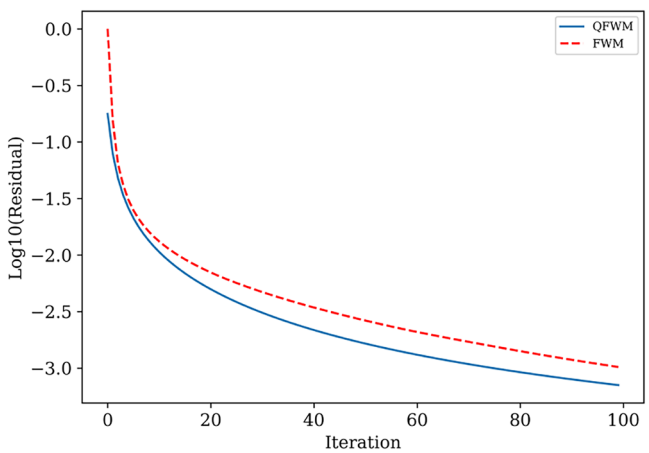

Figure 9 | Comparative analysis of the wavefield residual. Conventional FWM (red dashed) shows higher residuals, while Q-FWM (light blue solid) reduces them.

In our initial experiment, we evaluated the proposed gradient-based method for updating the Q_f values. In this test, we assumed that the correct reflectivity and velocity models were known and provided, and the inversion was performed solely for Q_f updating. The initial Q_f model was set to a constant value of 100 at all depth levels. Figure 5 presents the estimated Q_f model after 100 iterations. As shown, the estimated Q_f model closely matches the true Q_f model. Notably, after approximately 50 iterations, the Q_f model exhibited no significant changes; however, the inversion was continued to 100 iterations to ensure convergence of the algorithm and to confirm that it does not overcompensate for the attenuation effect.

The first experiment focused exclusively on testing the gradient-based procedure for updating Q_f. In the following two experiments, we evaluated the complete method. In the first, we applied the conventional FWM method to estimate reflectivity, assuming no attenuation (i.e., high Q_f values). In the second, we performed the test using our Q-FWM method, which simultaneously estimates both reflectivity and the Q_f model. Figure 6 presents a comparison between the standard FWM and the proposed Q-FWM results. The Q-FWM method yields a noticeably more

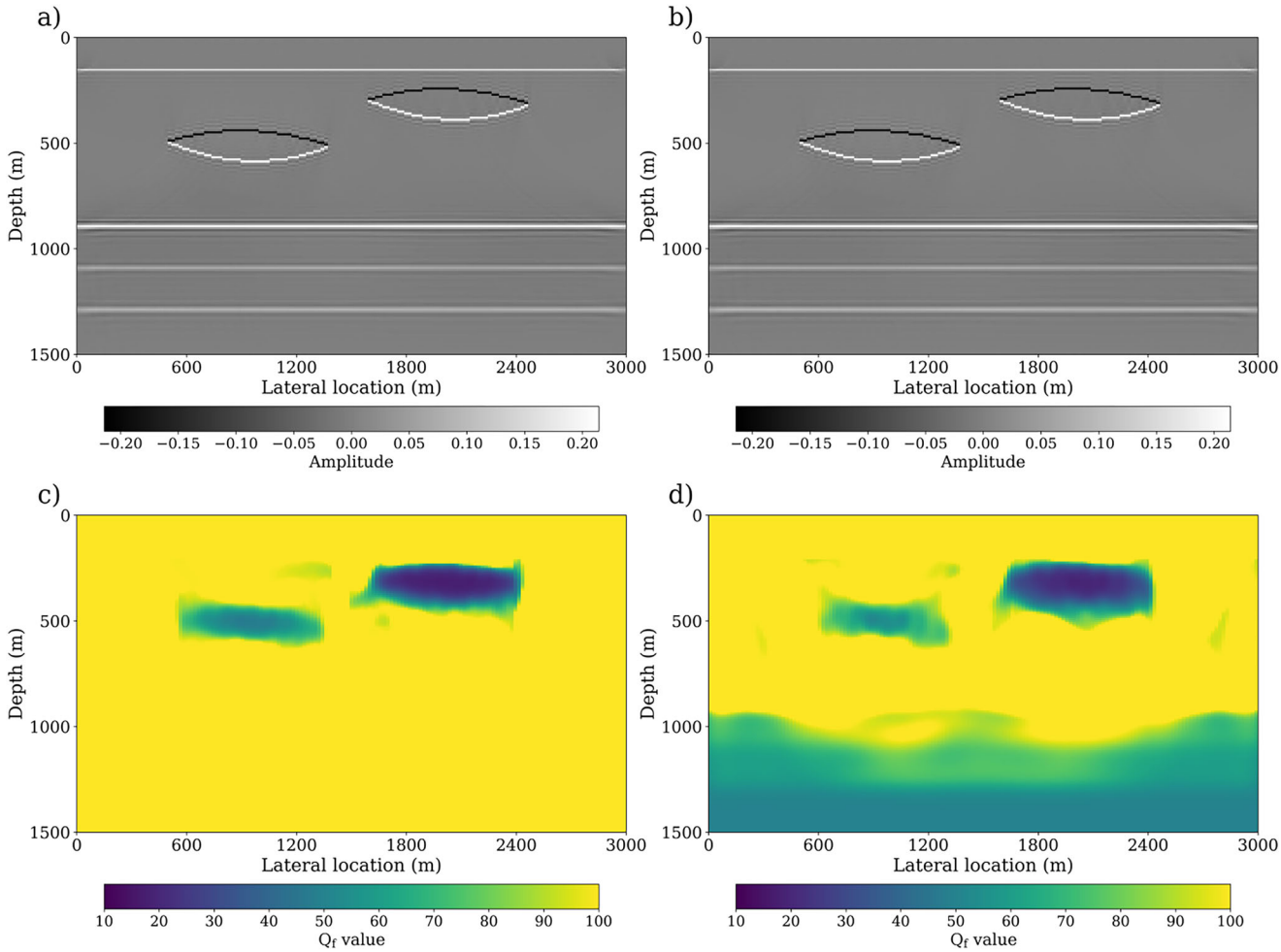

Figure 10 | Estimated images (top row) and corresponding Q_f models (bottom row) obtained using different initial attenuation models. Panels (a) and (c) correspond to a nearly lossless initialization (e.g., Q_f=100), while panels (b) and (d) correspond to a low-Q_f initialization ($Q_f = 50$).

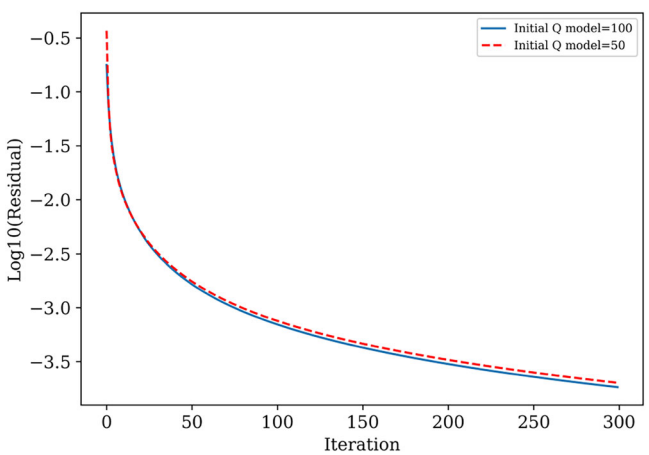

Figure 11 | Comparative analysis of the wavefield residual obtained using different initial attenuation models. The residual evolution indicates consistent and stable convergence for both tested initializations.

accurate reflectivity estimate, particularly in regions affected by attenuation (Figure 6a). In the absence of attenuation compensation (i.e., without incorporating Q_f), energy loss effects are imprinted on the reflectors, thereby reducing image resolution. This is especially evident in Figure 6a, where the reflectors beneath the lens-shaped anomalies exhibit diminished continuity and amplitude, leading to increased ambiguity in the recovered reflectivity. These artefacts arise from the inability of the standard FWM to account for attenuation. Figure 7 shows a reflectivity comparison among FWM, Q-FWM, and the true reflectivity for the same lateral position. The Q-FWM trace displays improved agreement with the true reflectivity in deeper intervals affected by strong attenuation, whereas the FWM result exhibits more pronounced amplitude decay. These results further support the effectiveness of Q-FWM for amplitude recovery at depth. The estimated Q_f values after 100 iterations are shown in Figure 8. The inverted Q_f model obtained from the Q-FWM method closely reproduces the true Q_f distribution, demonstrating the reliability of the proposed inversion scheme. Figure 9 compares the residuals obtained using FWM and Q-FWM. The residuals associated with Q-FWM are noticeably lower than those from the conventional FWM that neglects attenuation. This reduction indicates that incorporating Q_f modelling and compensation improves the data fit by effectively accounting for attenuation effects.

To analyse the convergence behaviour of the proposed method and its sensitivity to the initial attenuation model, additional experiments were conducted using two different initial Q_f

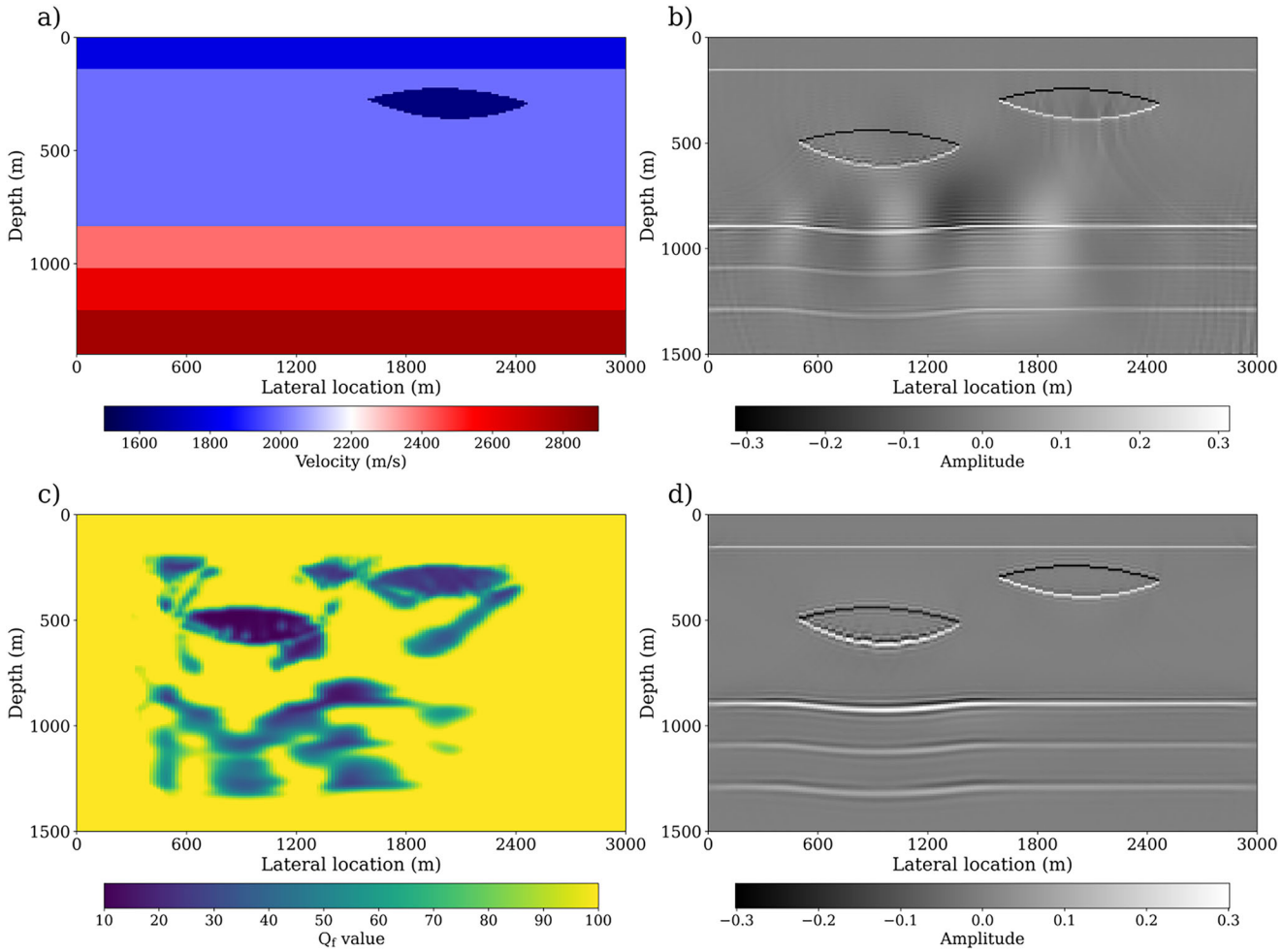

Figure 12 | Velocity sensitivity experiment. (a) Perturbed velocity model used as the input. (b) Migrated image obtained using conventional FWM. (c) Estimated Q_f model obtained during the inversion. (d) Migrated image obtained using the proposed Q-FWM method.

models: a nearly lossless case ($Q_f = 100$), similar to the model used in the previous experiment and a strongly attenuative case ($Q_f = 50$). In both scenarios, the inversion was run for 300 iterations and the data residual was monitored at each iteration. The convergence curves (Figure 11) show a consistent and monotonic decrease in the residual for both initial models, indicating stable convergence behaviour. When starting from an incorrect low-Q_f model, the algorithm is still able to recover towards a more accurate attenuation representation, although the convergence rate is slower compared to the lossless initialization. The corresponding estimated images and estimated Q_f models are shown in Figure 10. In the low-Q_f initialization case, the estimated Q_f model converges more slowly towards the true attenuation values, particularly in regions with weaker wavefield illumination, where the sensitivity to attenuation is reduced. Note that Figure 10c is done with extra 200 iterations – somewhat improved compared to the result in Figure 8. These observations suggest that while the proposed method is robust to inaccuracies in the initial attenuation model and does not exhibit signs of being trapped in local minima for the tested scenarios, assuming a weakly attenuative medium or a relatively high initial Q_f model can improve convergence speed and reduce the number of required iterations.

Next, we investigate the sensitivity of the proposed Q-FWM method to velocity errors. In the previous experiments, the true velocity model was used during migration. However, in practical applications, the velocity model is rarely known exactly. To evaluate the robustness of the method, we repeat the imaging experiment using a perturbed velocity model. The perturbed velocity model is shown in Figure 12a. In the true model, two lens-shaped velocity anomalies are present, one on the left side and one on the right side of the model. In this experiment, the velocity associated with the left lens-shaped anomaly is intentionally replaced by the background velocity, while the velocity of the right anomaly remains unchanged. The initial Q_f model is set to (Q_f = 100) throughout the model, consistent with the first experiment. The migrated image obtained using conventional FWM is shown in Figure 12b, the estimated Q_f model is presented in Figure 12c and the image obtained using the proposed Q-FWM method is shown in Figure 12d. As expected, the velocity error degrades the imaging results for both methods. Although neither image is as well focused as the results obtained using the correct velocity model, the image produced by Q-FWM remains noticeably more focused than that obtained using FWM. However, the reflectors associated with the left lens-shaped anomaly and the deeper reflectors beneath this structure are not positioned correctly as expected due to the velocity inaccuracies. Because the proposed

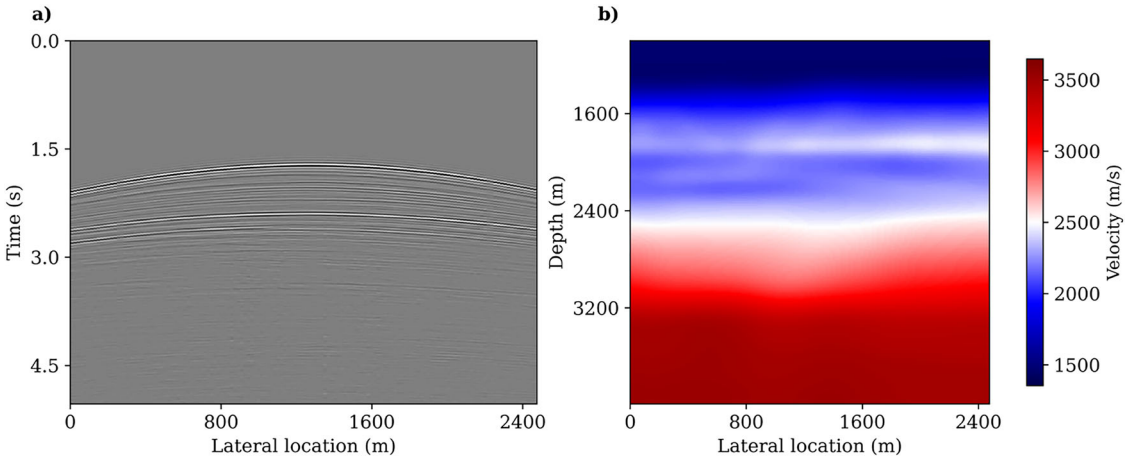

Figure 13 | Data from the Vøring Basin after preprocessing. (a) One measured shot record after basic preprocessing and (b) corresponding velocity model.

method estimates the Q_f model in a tomographic manner, the velocity error in the left lens anomaly affects the estimated Q_f distribution over a broader region of the model. In particular, the estimated Q_f values associated with the left lens-shaped anomaly are lower than the corresponding values in the true Q_f model. This influence also propagates to neighbouring regions, causing the estimated Q_f values in other parts of the model to be generally lower than the true values. Velocity inaccuracies may also affect attenuation estimation in conventional approaches such as the spectral ratio method, primarily through errors in travel-time differences and event alignment. This behaviour, therefore, reflects a general limitation in attenuation estimation. In addition, this effect influences the Q_f estimation associated with the right lens-shaped anomaly, where the recovered Q_f values become higher than the true values in that region. Although the estimated Q_f values are less accurate than those obtained in the first experiment with the correct velocity model, the method is still able to detect the main Q_f anomalies in the model. Despite these inaccuracies in the estimated Q_f distribution, the final migrated image remains interpretable and the overall imaging result can still be considered acceptable.

6.2 | Field Data Example

To further demonstrate the effectiveness of the proposed Q-FWM scheme, we demonstrate the proposed method on a 2D field dataset from the Vøring basin. The data were acquired by a streamer survey in the North Sea, in the Vøring area, offshore Norway. The source and receiver spacings used in our example are 50 and 25 m, respectively. Several preprocessing steps have been applied to the data, including the direct wave and surface-related multiple removals, deghosting, near-offset interpolation and using reciprocity to make the shot records split spread. The source wavelet was estimated from the surface-related multiples by using a so-called estimation of primaries by the sparse inversion process (van Groenestijn and Verschuur 2009). Figure 13 shows a one-shot record of the data after preprocessing (Figure 13a) and the corresponding velocity model (Figure 13b). The frequency bandwidth during FWM and Q-FWM is 5–30 Hz.

The test was performed under three distinct conditions. In the first case, the conventional FWM method was applied to estimate reflectivity, under the assumption of negligible attenuation (i.e., high Q_f values). In the second case, the proposed Q-FWM method was employed to simultaneously estimate both the reflectivity and the Q_f model, assuming that the data contained only primary reflections. Finally, the third case involved applying Q-FWM while accounting for both primary reflections and internal multiples present in the data. For the Q-FWM tests, the upper and lower bounds of the inverted Q_f values were set to 100 and 10, respectively. The initial Q_f model was set to a constant value of 100 for the entire dataset. The water layer at the top was treated as non-attenuative, and during the updating process the Q_f values for the water layer were excluded from the inversion. The inversion was stopped once the residuals ceased to decrease significantly.

The estimated reflectivity models obtained from the three test cases are presented in Figure 14. As shown, the Q-FWM result (Figure 14b,c) demonstrates a noticeable improvement in image resolution compared to the conventional FWM result (Figure 14a). The enhanced recovery of high-frequency components in the compensated image leads to improved event resolution. Additionally, the correction of attenuation-induced phase distortions increases event coherency, resulting in more laterally continuous and geologically consistent reflectors. Furthermore, when internal multiples are incorporated in the final test (Figure 14c), the estimated reflectivity exhibits an additional enhancement. The regions of improvement are indicated by dashed ellipses, highlighting areas where the structural detail is better resolved relative to the previous cases. Although the improvement between Figure 14b and 14c is not easily distinguished by visual inspection, the difference plot in Figure 14d clearly highlights the regions where the inclusion of internal multiples provides additional resolution. Figure 15 shows the inverted Q_f models for the Q-FWM case, considering only primary reflections and for the case incorporating both primaries and internal multiples, after 20 iterations of Q_f inversion. The estimated Q_f models in both cases are generally similar, though the Q_f values are slightly higher when multiples are included. This is because, when ignored, multiples are treated as attenu-

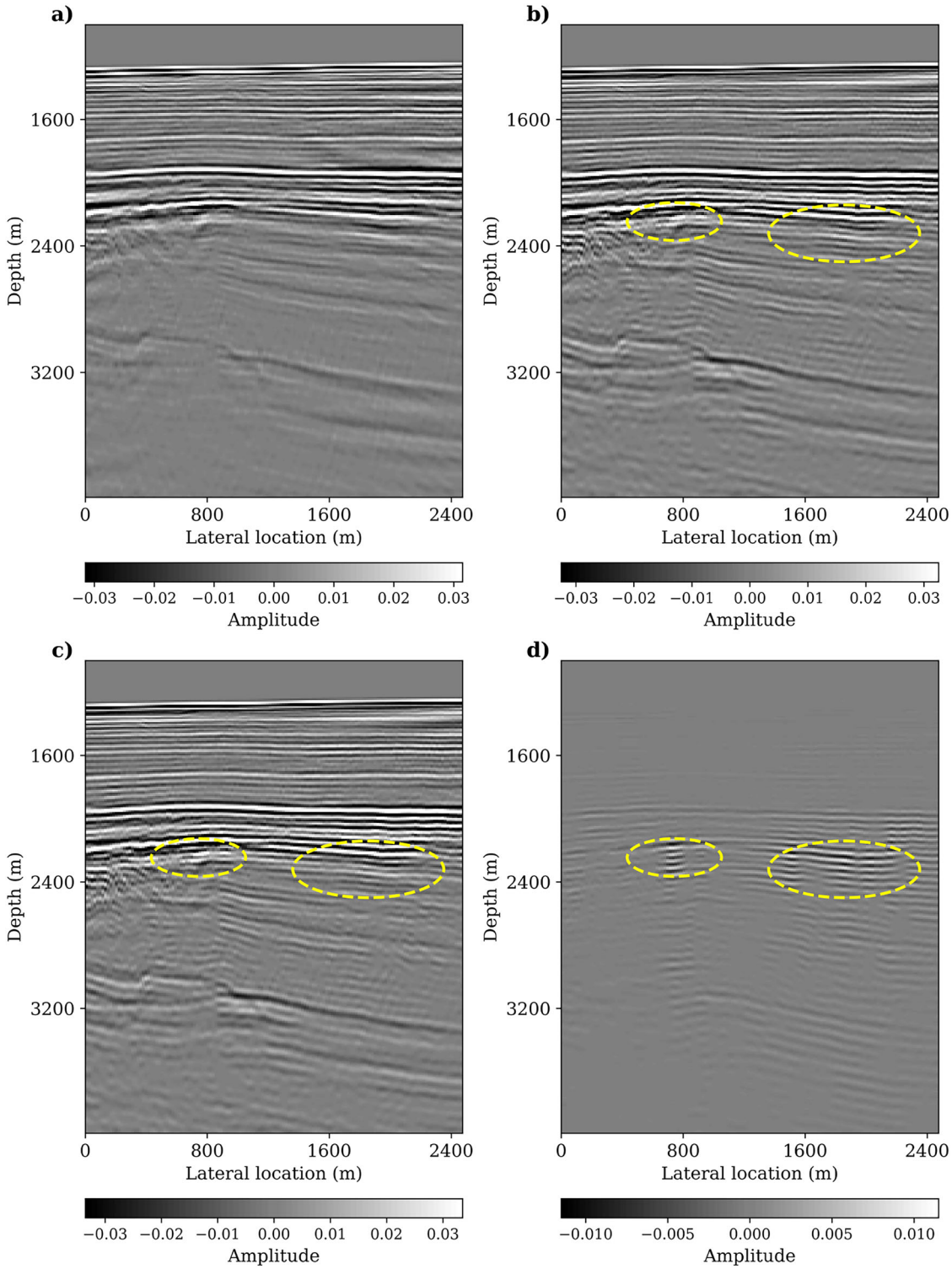

Figure 14 | Comparative analysis of reflectivity estimations. (a) Estimated reflectivity by FWM. (b) Estimated reflectivity by Q-FWM excluding internal multiples. (c) Estimated reflectivity by Q-FWM including internal multiples. (d) Difference between (c) and (b), showing the result of including transmission effects and internal multiples by Q-FWM. Dashed ellipses indicate areas of improvement when internal multiples are incorporated.

ated primaries, causing cross-talk with true attenuation effects; incorporating them yields more realistic Q_f estimates. In both cases, the inversion recovers the Q_f anomalies, whose locations agree with the geological interpretation as they coincide with low-velocity regions.

Figure 16 presents reflectivity comparisons extracted from vertical cross-sections at three representative lateral locations, comparing Q-FWM with primaries only and Q-FWM including internal multiples against the corresponding FWM results. In both scenarios, Q-FWM exhibits a pronounced improvement in amplitude recovery relative to FWM. While the inclusion of internal multiples

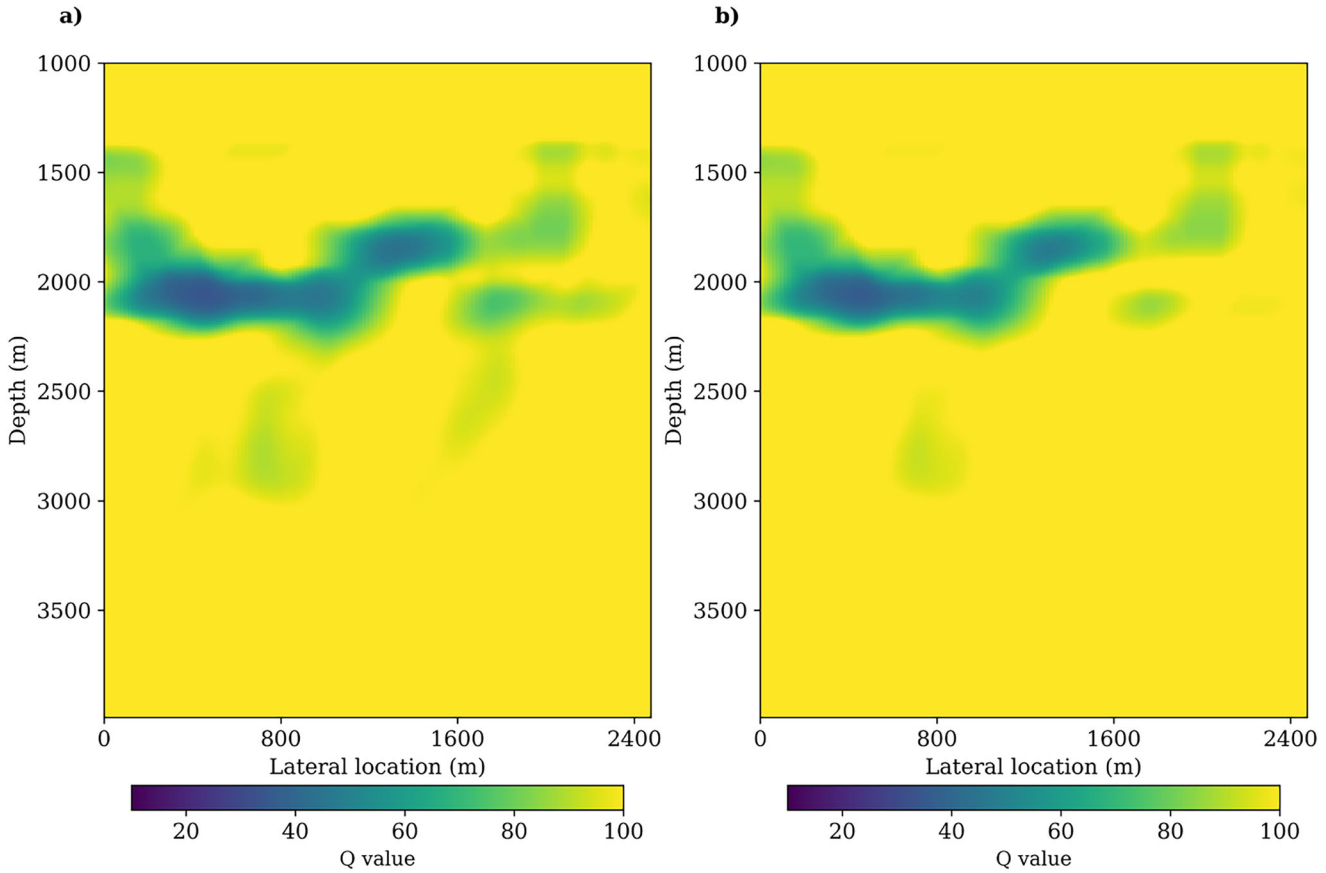

Figure 15 | Comparative analysis of quality factor estimations. (a) Q_f estimation result via Q-FWM excluding internal multiples. (b) Q_f estimation result via Q-FWM including internal multiples.

leads to a better overall fit, which is more clearly visible in the reflectivity images shown in Figure 14, the differences between the two Q-FWM variants in the single-trace comparisons are relatively subtle. Nevertheless, both cases are included here to provide a complete and consistent comparison.

Figure 17 compares the residuals obtained under the three testing conditions. The residuals from the second condition – Q-FWM with only primary reflections – and the third condition – Q-FWM including both primaries and internal multiples – are both noticeably lower than those from the first condition, which uses conventional FWM assuming negligible attenuation. This reduction indicates that incorporating Q_f modelling and compensation improves the data fit by mitigating attenuation effects. The residual curves for the second and third conditions are very close to each other, with the third condition yielding slightly lower residuals, suggesting a modest additional improvement when internal multiples are included.

7 | Discussion

Regarding computational cost, incorporating attenuation into the migration algorithm increases the computational cost relative to the original method. Across multiple datasets, the attenuation-aware algorithm requires approximately 4–8× more computational effort than the original formulation, depending on the model complexity and data size. This increase arises from the additional calculations needed to model amplitude decay and attenuation effects. In addition to amplitude decay, our formulation accounts for the dispersive phase behaviour that accompanies attenuation in viscoacoustic media. Because attenuation and dispersion are linked through the Kramers–Kronig relations, incorporating both effects ensures that the forward modelling operator remains physically consistent and causal. Despite the higher computational cost, the proposed method yields substantially improved accuracy and physical realism in the migrated results, particularly in terms of amplitude behaviour in highly attenuated regions. Representing both amplitude and phase effects of attenuation also improves the consistency between modelled and observed wavefields, which is particularly important in waveform-based inversion and imaging frameworks. Consequently, the increased computational expense is justified by the improved fidelity of the results.

Although we presented a limited number of examples, the results demonstrate the principle that using full-waveform matching within a depth-imaging framework can map Q_f effects in a tomographic sense, even in cases where there are local (lateral and vertical) variations. This capability becomes particularly advantageous when attenuation varies laterally and vertically, since the proposed framework estimates Q_f as a spatially distributed parameter within a wave-equation-based inversion rather than as a localized measurement along individual ray paths. Mapping Q_f effects in a tomographic sense is generally not possible with traditional methods, such as the spectral ratio

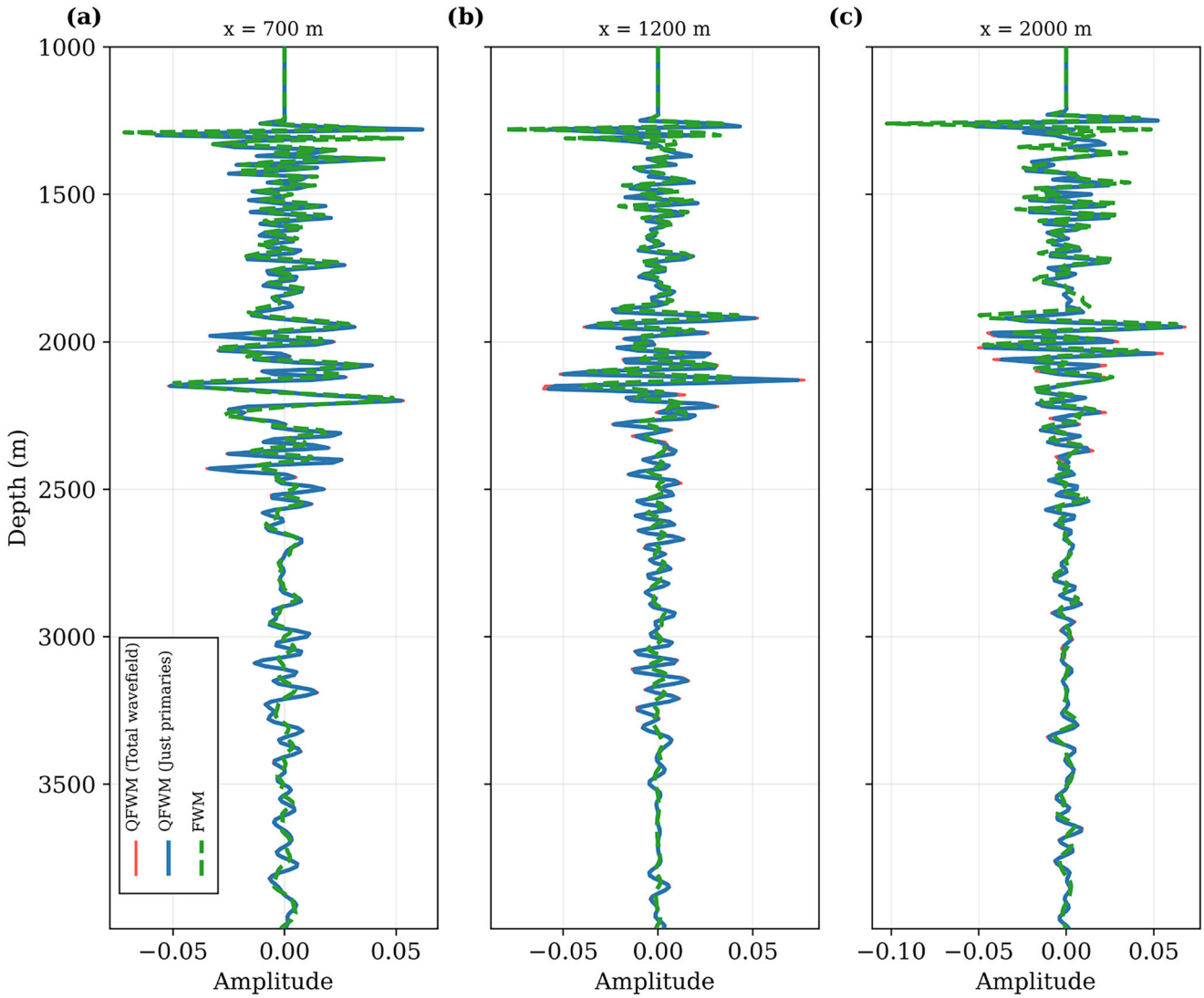

Figure 16 | Comparative analysis of reflectivity estimations from vertical cross-sections at three representative lateral locations.

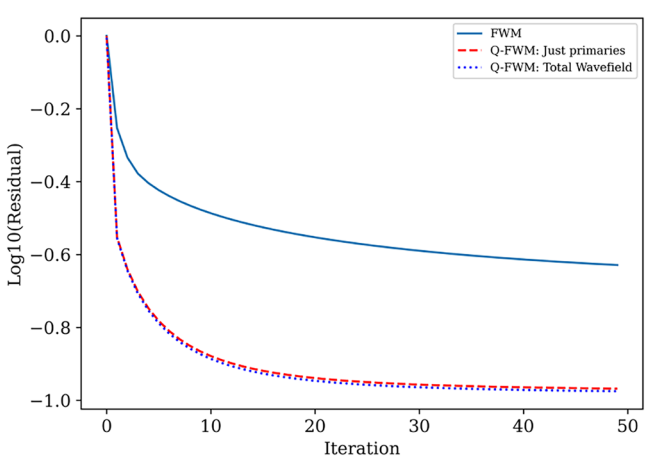

Figure 17 | Comparative analysis of the wavefield residual. Conventional FWM (light blue solid) shows higher residuals, while Q-FWM with primaries (red dashed) reduces them significantly. Q-FWM with the total wavefield (dark blue dotted) achieves the lowest residuals, with a slight further reduction compared to primaries only.

or CFS approaches, because these methods typically operate in the measurement domain without reconstructing spatially distributed attenuation models. Conventional amplitude-based approaches infer attenuation from spectral amplitude decay along assumed propagation paths and therefore rely on simplified propagation assumptions that may break down in complex geological environments. This distinction highlights the conditions under which the proposed approach provides the greatest benefit, particularly in the presence of spatially varying attenuation and complex wave propagation effects. We also realize that the accuracy of the estimated Q_f effects can be influenced by errors in the background velocity model. To evaluate this sensitivity, we performed an additional experiment using a perturbed velocity model, as discussed in the results section. The results show that velocity inaccuracies can introduce biases in the estimated Q_f distribution and reduce the focusing of the migrated image. Nevertheless, the main attenuation anomalies are still detected and the resulting image remains interpretable. This behaviour is not unique to the proposed method, as velocity errors can also affect attenuation estimates in conventional approaches. We see it as a logical next step to perform a joint inversion of background velocity and Q_f, but leave this for future work. A joint inversion

framework may further improve the robustness of the attenuation estimates in complex settings where velocity and attenuation effects are coupled in the observed wavefield. Another interesting aspect to mention is the effect of internal multiples: if internal multiples are generated at a sub-seismic scale, these multiples are not resolvable by the full wavefield modelling process but can contribute to the observed Q_f effects (O'Doherty and Anstey 1971). However, when the multiple-generating reflectors become more widely separated, the multiple-generating process becomes more deterministic and they can be described by the FWMod process. In this way, multiples at both seismic and sub-seismic scales can be handled naturally by our proposed method. Because the proposed framework relies on wave-equation-based forward modelling, it can naturally account for complex propagation effects such as multi-pathing, scattering and internal multiples, which are difficult to accommodate in amplitude-only Q_f estimation methods.

The adopted one-way modelling engine is very suitable to include the Q_f effects for both the forward modelling and the gradient calculation. This formulation also enables attenuation and its associated dispersion to be incorporated directly in the propagation operator, allowing these effects to be handled consistently within the waveform-matching inversion framework. However, it is well-known that using the one-way propagators has limitations, such as the inability to image reflectors close to 90 degrees and beyond, as well as turning waves. Thus, our proposed method – despite being effective and flexible – would not apply to all geologic scenarios, such as sub-salt imaging. But in favour of our proposed method is the possibility to adopt different Q_f models in the propagator and the option to include/exclude internal multiples during the imaging process. With time-domain two-way wave-equation modelling engines, it is well-known that bringing in accurate Q_f models (obeying the causality relationship) is not trivial and can also become computationally more intensive (Ursin and Toverud 2002; Zhu et al. 2013). At the same time, in relatively homogeneous media with weak attenuation or limited bandwidth, simpler amplitude-only Q_f estimation approaches may still provide reasonable estimates at significantly lower computational cost. In such cases, the additional complexity of wave-equation-based inversion may offer limited practical benefit.

8 | Conclusions

We have presented an approach for incorporating both attenuation compensation and Q_f estimation into the FWM framework. In the FWM process, this integration can be seamlessly implemented within the forward modelling scheme, which is composed of distinct propagation and scattering operators. For Q_f estimation, we proposed a full-waveform matching strategy that utilizes residual data to accurately estimate Q_f and applies the corresponding compensation during migration. The method is implemented in the image domain within a wave-equation tomography framework and establishes a direct link between model perturbations and Q_f perturbations. Using a 2D synthetic example, we demonstrated that the proposed method can recover both an accurate reflectivity image and a reliable attenuation model. Application to field data further confirmed the effectiveness of the approach.

Acknowledgements

This work is carried out within the, Delphi Consortium and is partly funded by the European Union's Horizon 2020 Research and Innovation Programme under the Marie Sklodowska-Curie COFUND scheme with grant agreement No. 101034267 (ENGAGE). The authors thank Equinor for making the field data available.

Funding

This study was partly funded by the European Union's Horizon 2020 Research and Innovation Programme under the Marie Skłodowska-Curie COFUND scheme (grant agreement No. 101034267, ENGAGE) and by the sponsors of the Delphi Consortium.

Conflicts of Interest

The authors declare no conflicts of interest.

Data Availability Statement

The data that support the findings of this study are available from the corresponding author upon reasonable request.

References

Aki, K., and P. G. Richards. 2002. *Quantitative Seismology*. University Science Books.

Bai, J., and D. Yingst. 2013. "Q Estimation Through Waveform Inversion." In the *75th Annual International Conference and Exhibition, EAGE, Extended Abstracts, SPE EUROPEC*, cp-348-00601. European Association of Geoscientists & Engineers.

Berkhout, A. 2014a. "An Outlook on the Future of Seismic Imaging, Part I: Forward and Reverse Modelling." *Geophysical Prospecting* 62: 911–930.

Berkhout, A. 2014b. "An Outlook on the Future of Seismic Imaging, Part II: Full-Wavefield Migration." *Geophysical Prospecting* 62: 931–949.

Berkhout, A. 2014c. "An Outlook on the Future of Seismic Imaging, Part III: Joint Migration Inversion." *Geophysical Prospecting* 62: 950–971.

Berkhout, A. J. 1982. *Seismic Migration, Imaging of Acoustic Energy by Wave Field Extrapolation, A: Theoretical Aspects*. Elsevier.

Carcione, J. M. S. Picotti, D. Gei, and G. Rossi. 2006. "Physics and Seismic Modeling for Monitoring CO_2 Storage." *Pure and Applied Geophysics* 163: 175–207.

Carvalho Costa, J. C., and L. F. Gomes. 2011. "Limitations of Spectral Ratio and Centroid Frequency Shift Methods for Q Estimation in Heterogeneous Media." *Geophysical Prospecting* 59: 515–528.

Cheng, P., and G. F. Margrave. 2008. "Complex Spectral Ratio Method for Q Estimation." CREWES Research Report 20.

Claerbout, J. F. 1971. "Toward a Unified Theory of Reflector Mapping." *Geophysics* 36: 467–481.

Dasgupta, R., and R. A. Clark. 1998. "Estimation of Q From Surface Seismic Reflection Data." *Geophysics* 63: 2120–2128.

Davydenko, M., and D. Verschuur. 2017. "Full-Wavefield Migration: Using Surface and Internal Multiples in Imaging." *Geophysical Prospecting* 65: 7–21.

Dong, Y. J., Y. Shen, K. Guo, et al. 2025. "Characterization of Petrophysical and Seismic Properties for CO_2 Storage With Sensitivity Analysis." *Petroleum Science* 22, no. 1: 193–209.

Dutta, G. 2016. "Skeletonized Wave-Equation Inversion for Q." In the *86th Annual International Meeting, Expanded Abstracts* 3618–3623. SEG.

Dutta, G., and G. T. Schuster. 2016. "Wave-Equation Q Tomography." *Geophysics* 81: R471–R484.

Futterman, W. I. 1962. "Dispersive Body Waves." *Journal of Geophysical Research* 67: 5279–5291.

Gazdag, J. 1978. "Wave Equation Migration With the Phase-Shift Method." *Geophysics* 43: 1342–1351.

Gazdag, J., and P. Sguazzero. 1984b. "Migration of Seismic Data by Phase Shift Plus Interpolation." *Geophysics* 49: 124–131.

Gurevich, B., and R. Pevzner. 2015. "Frequency-Dependent Seismic Attenuation and Dispersion." *Geophysics* 80: WA147–WA155.

Hauksson, E., J. Andrews, and K. Hutton. 2006. "A Model of Attenuation Structure Beneath Southern California." *Journal of Geophysical Research: Solid Earth* 111: B05302.

Hedlin, M. 2006. "Husky Energy Attenuation Modeling." https://miis.maths.ox.ac.uk/183/1/husky_energy.pdf.

Hoogerbrugge, L., and E. Verschuur. 2021. "Including Converted Waves in Full Wavefield Migration." In the *82nd EAGE Annual Conference & Exhibition*, vol. 2021, 1–5. European Association of Geoscientists & Engineers.

Huang, C., T. Zhu, and G. Xing. 2023. "Data-Assimilated Time-Lapse Visco-Acoustic Full-Waveform Inversion: Theory and Application for Injected CO_2 Plume Monitoring." *Geophysics* 88: R105–R120.

Kamei, R., and R. G. Pratt. 2008. "Waveform Tomography Strategies for Imaging Attenuation Structure With Cross-Hole Data." In the *70th Annual International Conference and Exhibition, Extended Abstracts, SPE EUROPEC*, cp-40-00140. European Association of Geoscientists & Engineers.

Malinowski, M. 2012. "Anelastic Attenuation Factor." Accessed August 8, 2025. https://en.wikipedia.org/wiki/Anelastic_attenuation_factor.

Mateeva, A. 2003. "Thin Horizontal Layering as a Stratigraphic Filter in Absorption Estimation and Seismic Deconvolution." PhD diss., Colorado School of Mines.

Mittet, R., R. Sollie, and K. Hokstad. 1995. "Prestack Depth Migration With Compensation for Absorption and Dispersion." *Geophysics* 60: 1485–1494.

O'Doherty, R., and N. A. Anstey. 1971. "Reflections on Amplitudes." *Geophysical Prospecting* 19: 430–458.

Plessix, R. E. 2006. "Estimation of Velocity and Attenuation Coefficient Maps From Crosswell Seismic Data." *Geophysics* 71: S235–S240.

Qu, Y., Y. Wang, Z. Li, and C. Liu. 2021. "Q Least-Squares Reverse Time Migration Based on the First-Order Viscoacoustic Quasidifferential Equations." *Geophysics* 86: S283–S298.

Qu, Y., J. Zhu, Z. Chen, C. Huang, Y. Wang, and C. Liu. 2022. "Q-Compensated Least-Squares Reverse Time Migration With Velocity-Anisotropy Correction Based on the First-Order Velocity-Pressure Equations." *Geophysics* 87: S335–S350.

Quan, Y., and J. M. Harris. 1997. "Seismic Attenuation Tomography Using the Frequency Shift Method." *Geophysics* 62: 895–905.

Raji, W., and A. Rietbrock. 2013. "Attenuation (1/Q) Estimation in Reflection Seismic Records." *Journal of Geophysics and Engineering* 10: 045012.

Reine, C., R. A. Clark, and M. van der Baan. 2012. "Robust Prestack Q-Determination Using Surface Seismic Data: Part 2, 3D Case Study." *Geophysics* 77: B1–B10.

Rickett, J. 2007. "Estimating Attenuation and the Relative Information Content of Amplitude and Phase Spectra." *Geophysics* 72: R19–R27.

Safari, M., and D. Verschuur. 2024. "Using Internal Multiples for More Accurate Seismic Q Estimation." In the *85th EAGE Annual Conference & Exhibition (Including the Workshop Programme)*, vol. 2024, 1–5. European Association of Geoscientists & Engineers.

Safari, M., and D. Verschuur. 2025. "Robust Joint Imaging and Tomographic Q-Estimation Based on Full Wavefield Matching Using a Machine Learning Constraint." In the *86th EAGE Annual Conference & Exhibition*, vol. 2025, 1–5. European Association of Geoscientists & Engineers.

Safari, M., and J. Verschuur. 2023. "Joint Migration Inversion Including Q Effects: Towards Q Estimation." In the *84th EAGE Annual Conference & Exhibition*, vol. 2023, 1–5. European Association of Geoscientists & Engineers.

Shen, Y., B. Biondi, and R. Clapp. 2018. "Q-Model Building Using One-Way Wave-Equation Migration Q Analysis-Part 1: Theory and Synthetic Test." *Geophysics* 83: S93–S109.

Sheriff, R. E., and L. P. Geldart. 1995. *Exploration Seismology*, Cambridge University Press.

Staal, X., and D. Verschuur. 2013. "Joint Migration Inversion, Imaging Including All Multiples With Automatic Velocity Update." In the *75th EAGE conference & exhibition incorporating SPE EUROPEC 2013*, cp–348. European Association of Geoscientists & Engineers.

Toksöz, M., and D. Johnston. S. of Exploration Geophysicists. 1981. *Seismic Wave Attenuation*, Geophysics Reprint Series. Society of Exploration Geophysicists.

Tonn, R. 1991. "The Determination of Seismic Quality Factor Q From VSP Data: A Comparison of Different Computational Techniques." *Geophysical Prospecting* 45: 87–109.

Ursin, B., and T. Toverud. 2002. "Comparison of Seismic Dispersion and Attenuation Models." *Studia Geophysica et Geodaetica* 46: 293–320.

van Groenestijn, G. J. A., and D. J. Verschuur. 2009. "Estimation of Primaries and Near-Offset Reconstruction by Sparse Inversion: Marine Data Applications." *Geophysics* 74: A23–A28.

Verschuur, D., X. Staal, and A. Berkhout. 2016. "Joint Migration Inversion: Simultaneous Determination of Velocity Fields and Depth Images Using All Orders of Scattering." *The Leading Edge* 35: 1037–1046.

Wang, Y. 2008. "Q-Compensated Reverse-Time Migration." *Geophysics* 73: S1–S6.

Wang, Y. 2014. "Stable Q Analysis on Vertical Seismic Profiling Data." *Geophysics* 79: D217–D225.

Wang, Y., and S. Qu. 2022. "Q-Compensated Full Waveform Inversion for Velocity and Density." *Exploration Geophysics* 53: 512–526.

White, R. 1992. "The Accuracy of Estimating Q From Seismic Data." *Geophysics* 57: 1508–1511.

Xing, Y., J. Sheng, and L. Huang. 2019. "Modeling and Inversion of Attenuative Media Using a Frequency-Independent Q Approach." *Journal of Geophysical Research: Solid Earth* 124: 5647–5665.

Yu, Y., R. S. Lu, and M. M. Deal. 2002. "Compensation for the Effects of Shallow Gas Attenuation With Viscoacoustic Wave-Equation Migration." In the *SEG Technical Program Expanded Abstracts 2002*, 2062–2065. Society of Exploration Geophysicists.

Zhang, C. 2008. "Seismic Absorption Estimation and Compensation." PhD diss., University of British Columbia.

Zhang, Y., Z. Li, H. Chen, and X. Wang. 2024. "Ocean-Bottom Dual-Sensor Q-Compensated Elastic Least-Squares Reverse Time Migration Based on Viscoacoustic and Separated-Viscoelastic Coupled Equations." *Geophysics* 89: S1–S15.

Zhang, Y., R.-S. Wu, and G. Chen. 2015. "Estimating Seismic Attenuation From Frequency-Dependent Amplitude Decay." *Geophysics* 80: WA1–WA13.

Zhu, T., J. M. Carcione, and J. M. Harris. 2013. "Approximating Constant-Q Seismic Propagation in the Time Domain." *Geophysical Prospecting* 61: 931–940.

Appendix A: Linearization of the Propagation Operator and Gradient Derivation for Q_f

This appendix presents the intermediate steps for the linearization of the one-way propagation operator with respect to the attenuation parameter A and the derivation of the corresponding gradient used for updating Q_f.

A.1 | Linearization of the One-Way Propagator

The vertical wavenumber in the case f the adopted Q_f model is defined as

$$k_z(A) = \sqrt{\omega^2 s^2 \left(1 - \frac{A}{\pi} \ln \frac{\omega}{\omega_0}\right)^2 \left(1 + \frac{iA}{2}\right)^2 - k_x^2}. \tag{A.1}$$

For a depth step Δz, the one-way phase-shift propagator in the wavenumber-frequency domain is given by

$$W^-(A) = \exp(-i\, k_z(A)\, \Delta z). \tag{A.2}$$

Assuming a small perturbation ΔA around a background value A_{old}, a first-order Taylor expansion yields

$$W^-(A_{\text{old}} + \Delta A) \approx W^-(A_{\text{old}}) + \left[\frac{\partial W^-}{\partial A}\right]_{A_{\text{old}}} \Delta A. \tag{A.3}$$

A.2 | Derivative with Respect to A

Using the chain rule, the derivative of the propagator with respect to A can be written as

$$\frac{\partial W^-}{\partial A} = -i\, \Delta z\, \mathrm{e}^{-ik_z \Delta z} \frac{\partial k_z}{\partial A}. \tag{A.4}$$

Differentiating k_z with respect to A gives

$$\frac{\partial k_z}{\partial A} = \frac{k_0^2}{k_z} \left[-\frac{\ln(\omega/\omega_0)}{\pi} \left(1 - \frac{A}{\pi} \ln \frac{\omega}{\omega_0}\right) \left(1 + \frac{iA}{2}\right)^2 + \frac{i}{2} \left(1 - \frac{A}{\pi} \ln \frac{\omega}{\omega_0}\right)^2 \left(1 + \frac{iA}{2}\right) \right], \tag{A.5}$$

where $k_0 = \omega s$.

Substituting this expression into the previous equation and transforming back to the space domain yields the linearized perturbation operator

$$\vec{L}_{0j}^-(z_m, z_n) \approx \mathcal{F}_x^{-1} \left\{ -j\Delta z \left[\frac{k_0^2}{k_z} \left(1 - \frac{A}{\pi} \ln \frac{\omega}{\omega_0}\right) \left(1 + \frac{iA}{2}\right)^2 \left(\frac{\ln(\omega/\omega_0)}{\pi}\right)^2 + \frac{i}{2} \left(1 + \frac{iA}{2}\right) \left(1 - \frac{A}{\pi} \ln \frac{\omega}{\omega_0}\right)^2 \right]_{A_{\text{old}}} \mathrm{e}^{-jk_z \Delta z} \mathrm{e}^{-jk_x x_j} \right\}. \tag{A.6}$$

Note that the expression $\vec{L}_0^-$ is entirely defined within the background medium.

A.3 | Stabilization

The operator in Equation (A.6) becomes unstable when $k_z \to 0$, corresponding to near-horizontal propagation. To ensure numerical stability, we apply the following stabilized approximation:

$$\frac{1}{k_z} \approx \frac{k_z^*}{k_z^* k_z + \epsilon}, \tag{A.7}$$

where $(\cdot)^*$ denotes complex conjugation and ϵ is a small positive stabilization parameter. In this study, the stabilization parameter is defined as

$$\epsilon = \alpha_{\text{stab}}\, k_0^2, \tag{A.8}$$

where α_{stab} is a scalar and k_0 is the background wavenumber defined earlier. This formulation provides a physically scaled stabilization that prevents numerical instabilities when k_z becomes small while avoiding excessive damping of the operator.

To determine an appropriate value for the scalar α_{stab}, we tested $\alpha_{\text{stab}} = 0.1$, 0.01 and 0.001. For all tested values, the inversion results and the recovered Q_f models were essentially identical, indicating that the proposed method is insensitive to the stabilization parameter within this range. Based on these observations, we adopt $\alpha_{\text{stab}} = 0.01$ for all experiments reported in this study. Thus, using this stabilization, Equation (A.6) transforms into

$$\vec{L}_{0j}^-(z_m, z_n) \approx \mathcal{F}_x^{-1} \left\{ -j\Delta z\, k_0^2 \frac{k_z^*}{k_z^* k_z + \epsilon} \left[\left(1 - \frac{A}{\pi} \ln \frac{\omega}{\omega_0}\right) \left(1 + \frac{iA}{2}\right)^2 \left(\frac{\ln(\omega/\omega_0)}{\pi}\right)^2 + \frac{i}{2} \left(1 + \frac{iA}{2}\right) \left(1 - \frac{A}{\pi} \ln \frac{\omega}{\omega_0}\right)^2 \right] \mathrm{e}^{-jk_z \Delta z} \mathrm{e}^{-jk_x x_j} \right\}. \tag{A.9}$$